3D zero-thickness coupled interface finite element: Formulation and application

B.Cerfontaine[a], A.C. Dieudonné[a,b], J.P. Radu[a], F. Collin[a,*], R. Charlier[a]

[a] *University of Liege, Geomechanics and Engineering Geology, Chemin des chevreuils, Liege, Belgium*
[b] *F.R.I.A., Fonds de la Recherche Scintifique - FNRS, Brussels, Belgium*

Abstract

In many fields of geotechnical engineering, the modelling of interfaces requires special numerical tools. This paper presents the formulation of a 3D fully coupled hydro-mechanical finite element of interface. The element belongs to the zero-thickness family and the contact constraint is enforced by the penalty method. Fluid flow is discretised through a three-node scheme, discretising the inner flow by additional nodes. The element is able to reproduce the contact/loss of contact between two solids as well as shearing/sliding of the interface. Fluid flow through and across the interface can be modelled. Opening of a gap within the interface influences the longitudinal transmissivity as well as the storage of water inside the interface. Moreover the computation of an effective pressure within the interface, according to the Terzaghi's principle creates an additional hydro-mechanical coupling. The uplifting simulation of a suction caisson embedded in a soil layer illustrates the main features of the element. Friction is progressively mobilised along the shaft of the caisson and sliding finally takes place. A gap is created below the top of the caisson and filled with water. It illustrates the storage capacity within the interface and the transversal flow. Longitudinal fluid flow is highlighted between the shaft of the caisson and the soil. The fluid flow depends on the opening of the gap and is related to the cubic law.

Keywords: Contact Mechanics, Interfaces, Finite elements, Offshore Engineering, Hydro-mechanical couplings
2010 MSC: 00-01, 99-00

List of symbols

Roman symbols

$(\mathbf{e}_1^1, \mathbf{e}_2^1, \mathbf{e}_3^1)$	local system of coordinates defined on mortar side
$(\mathbf{E}_1, \mathbf{E}_2, \mathbf{E}_3)$	global system of coordinates
f_{wl}	longitudinal fluid flux within the interface

[1] Contact email: f.collin@ulg.ac.be

f_{wt}	transversal fluid flux across the interface
$\mathbf{F}_E$, $\mathbf{F}_I$, $\mathbf{F}_{OB}$	external, internal and Out of balance energetically equivalent nodal forces
g_N, $\dot{\mathrm{g}}_N$	gap function, variation of this function
$\dot{\mathrm{g}}_T$	variation of tangential displacement
$\mathbf{J}$	jacobian of the transformation from actual to isoparametric element
k	intrinsic permeability
$\mathbf{K}$	stiffness matrix
$\mathrm{K}_N, \mathrm{K}_T$	penalty coefficients
p_N, p'_N	contact pressure, effective contact pressure
$\mathbf{R}$	rotation matrix
$\dot{\mathrm{S}}$	storage
$\mathbf{t}$	local contact stress vector
T_{wt}	transversal conductivity
$\mathbf{u}$	vector of generalised coordinates $(\mathrm{x}, \mathrm{y}, \mathrm{z}, \mathrm{p}_w)$
W	Gauss weight

Greek symbols

Γ_c^1	area of contact
$\Gamma_{\tilde{q}}^1$	area of the non-classical fluid boundary condition
$\delta\dot{\mathbf{x}}$	virtual field of velocities
$\delta\mathrm{p}_w$	virtual field of fluid pressures
$\boldsymbol{\epsilon}$	deformation tensor
μ	friction coefficient
ρ_w	fluid density
$\boldsymbol{\sigma}$	stress tensor
τ	tangential contact shear stress
$\phi^i(\xi, \eta)$	interpolation function related to node i, in the isoparametric system of coordinates
Ω^i	porous medium nb. i, Solid nb. i

Mathematical symbols

$\boldsymbol{\nabla}$	gradient operator
:	tensor contraction
$\cdot$	scalar product
$[\cdot]^T$	transpose operator
$[\cdot]^{-1}$	inverse operator
$\| \cdot \|$	norm
δ_{ij}	kronecker delta

1. Introduction

The role of interfaces and discontinuities is crucial in many fields of geotechnical engineering and engineering geology. They cover a wide range of scales from soil-structure interaction to geological faults. In all cases, the interface delineates two distinct media and has a very thin width with respect to them. They often constitute preferential paths for fluid flows, deformation and failure. Therefore the modelling of their behaviour is a major issue for engineers.

Assessing the behaviour of foundations requires a deep understanding of the interface mechanisms. Prediction of the frictional strength of a pile is crucial to estimate and model its resistance to driving [1, 2, 3]. Soil-foundation friction is also a major component of the resistance of anchors or pile foundations to pull loading [4, 5, 6]. The modelling of limit states or post-failure behaviours of these foundations requires specific numerical tools able to take into account large relative displacements between the foundation and the surrounding soil. Suction caissons or bucket foundations are a particular case of anchors. They may be used as permanent foundations for offshore structures [7, 8, 9]. They consist of steel cylinders open towards the bottom. They are installed within the soil by suction [10, 11], *i.e.* the water inside the caisson is pumped out creating a fluid flow from outside. This creates a differential of water pressure between inside and outside, digging the caisson into the soil. This suction effect is also mobilised during the loading of the foundation especially in traction [4, 12]. It increases the total transient resistance of the foundation. It also ensures the foundation does not fail even after full mobilisation of friction between the soil and the caisson. Correctly representing the large uplifting of the caisson and the mobilisation of friction are among the main challenges of their modelling [13, 14].

The behaviour of geological faults in the vicinity of hydrocarbon production wells was given much attention [15, 16]. Disturbances created by such a process may affect the environment in triggering micro-earthquakes or inducing settlements. Recently the possibility of carbon dioxide geological storage in reservoirs has given a new impetus to this topic [17, 18]. The fault opening may create a leakage path from the storage, fracture the caprock [19] or trigger earthquakes [20].

From the numerical point of view, the problem of contact between two solids are early developed. The first purely mechanical finite element of contact between two solids was early developed [21]. It allows these solids to get into contact or to loose contact during a simulation. The main concepts of this field are established during the eighties [22, 23, 24, 25] and consolidate during the nineties [26, 27, 28, 29, 30]. Many authors developed these elements in the mechanical field of research and especially metal forming [31, 32, 33].
Rock and soil mechanics largely contribute to constitutive modelling of interfaces [34, 35, 36]. The first improvement is the development of non-linear mechanical constitutive laws characterising rock joints or soil-structure interface. Criteria defining the maximum friction available and stress-strain relations are developed in [35, 37, 38, 39]. A special attention is paid to the characterisation

of shear-induced dilatancy [35, 40, 41]. The second improvement is the definition of experimental relations characterising the fluid flow within the rock joints [42, 43]. Coupled finite elements combine these two ingredients. They include hydro-mechanical [44, 45, 46, 47] or multi-phase couplings [48]. They take into account the fluid or multiphasic flow across and within the interface and its effect on the normal pressure acting on the joint.

The purpose of this paper is to present a versatile formulation of a fully coupled hydro-mechanical finite element of interface applicable to 3D simulations. It allies a mechanical large displacement formulation of a zero-thickness interface element with the modelling of fluid flow using a three-node strategy. This strategy discretises the field of fluid pressure on each side of the interface and inside it. Thence, the transversal fluid flow creates a drop of pressure across the interface. The element is hydro-mechanically coupled through the definition of an effective contact pressure, the fluid storage due to the gap opening and the variation of the interface longitudinal permeability with gap variation.

The originality lies in the coupling of the longitudinal and transversal flows within the interface to a classical formulation of mechanical contact in large displacements. Particularly this flow problem is also tackled in case of contact loss and large tangential displacements. Moreover both mechanical and flow problems are treated within a unique finite element code `LAGAMINE` developed at the university of Liege [49, 50]. This paper focuses on the general framework of the finite element of interface. However the formulation is very versatile and any constitutive law describing both mechanical and flow behaviours can be introduced instead of the proposed ones. An original application to the large uplift simulation of a suction caisson is provided to illustrate the capacities of the finite element of interface.

This paper is subdivided into four main parts. The first part describes the basics of interface finite elements. It explains the different ways to tackle and discretise mechanical contact and fluid flow within interfaces. The second part sets out the governing equations of the coupled problem and its continuum formulation. The third part displays the discretisation of this continuum formulation into finite elements. It consists of the definition of energetically equivalent nodal forces and stiffness matrix. Finally the last part describes the pull simulation of a suction caisson embedded in a soil layer. This application illustrates all the features of the interface element.

2. Review of interface finite elements

Coupled interface elements involve two distinct but related issues: the mechanical and the flow problems. The former describes the detection or the loss of contact between two bodies, the shearing of this contact zone... The flow problem describes the fluid flow within the interface created by the vicinity of fluid flows within porous media. These two problems are coupled since the fluid flow influences the opening of the discontinuity and its transmissivity. Moreover

the fluid flow across the interface creates a transversal drop of pressure between two porous media.

Numerically, two approaches exist within the framework of the finite element method to manage the mechanical contact between two bodies as shown in Figure 1. In the former approach, the interface zone is represented by a very thin layer of elements specially designed for large shear deformation [51, 52, 53]. The second approach, adopted in the following, involves special boundary elements. These elements have no thickness and are termed *zero-thickness* finite elements. They discretise the probable zone of contact and are activated only in that case. These elements are suitable for the modelling of large displacement and no remeshing technique is necessary. They are quite common in mechanics [21, 31, 36, 33, 54].

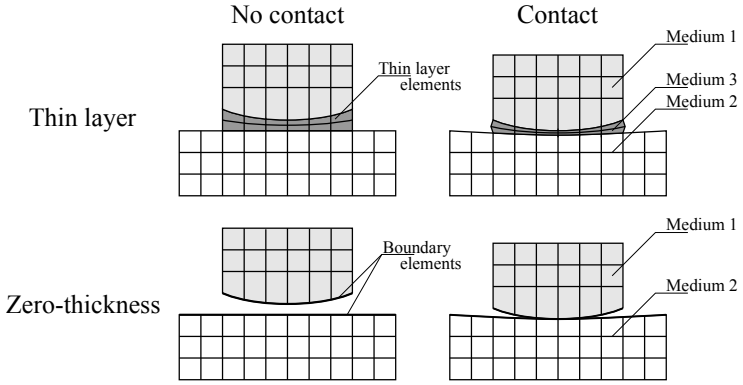

Figure 1: Comparison between thin layer and zero-thickness approaches in case of Hertzian contact.

Basically three ingredients are necessary to develop such an approach

- a scheme to enforce the normal contact constraint;
- a technique to discretise the contact area between solids and to compute a gap function g_N;
- a constitutive law to rule the normal/tangential behaviour.

The normal *contact constraint* ensures two solids in contact cannot overlap each other, the gap function is null, *i.e.* $\mathrm{g}_N = 0$. This contact gives birth to normal pressure on each side of the interface p_N and both solids deform. A physical constitutive law can rule this normal behaviour. The macroscopic relation between normal stress and deformation of the contact area depends on the microscopic geometry. For instance, in rock mechanics, the stress-displacement relation is non-linear [37] and depends on the deforming asperities as shown in Figure 2. In such a case, the interpenetration of the solids in contact have a physical meaning, *i.e.* $\mathrm{g}_N < 0$.

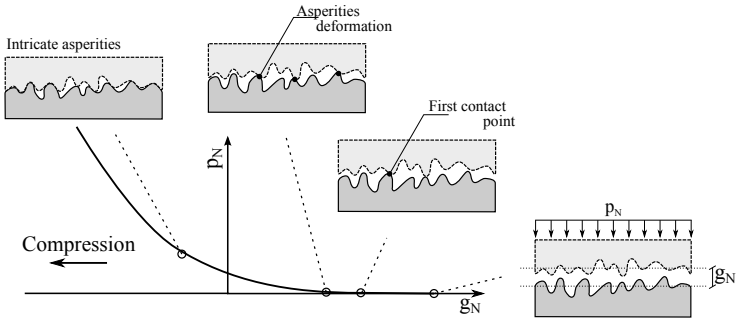

Figure 2: Constitutive law describing the normal behaviour of a rough rock joint. Normal pressure p_N depends on the deformation of asperities and closing of the gap g_N.

On the other hand, the normal constraint condition can be ensured on a purely geometrical basis, namely the interpenetration of the two solids is not allowed. This is physical only in case of perfectly smooth surfaces. The *Lagrange multiplier* method exactly ensures this condition [54]. It introduces additional variables, the Lagrange multipliers, corresponding to the contact pressures. The *penalty* method [33] regularises the constraint by authorizing an interpenetration of the solids in contact independently on the roughness of the surfaces. The related pressure is a function of the interpenetration through the penalty coefficient. Therefore the stress-displacement relation looses its physical basements [55]. Both Lagrangian and penalty solutions are identical for infinite penalty coefficient [56]. The main advantage is the simplicity of the method. The inconvenient is the risk of ill conditioning of the stiffness matrix. Both techniques are compared in Figure 3.

The available maximum friction may also evolve with the relative tangential displacement. In this case, a constitutive law ruling friction angle within the interface is also necessary. Dilatancy of the interface is also a crucial issue. This was extensively studied in case of rock joints [57, 58] and soil-structure interfaces [40, 41].

The contact constraint is a continuous condition over the boundary. Its discretisation in finite elements strongly impacts the performance of the computation. The *node-to-node* discretisation is the simplest one [24], as it is described in Figure 4. In this case, the contact constraint is imposed on a nodal basis. The gap and contact forces are computed between each pair of nodes. This formulation is dedicated to small relative displacements only.

The *node-to-segment* discretisation overcomes this drawback [59]. The contact constraint is applied between the nodes of one side of the interface, termed *slave surface* and the segments of the other side, termed *master surface*. The gap function is computed through the projection of the slave node onto the master surface. Such discretisation is sensitive to sudden change in projection direction between two adjacent segments and is improved by smoothing techniques [30].

The *segment-to-segment* discretisation [33, 60, 61] is based on the mortar method

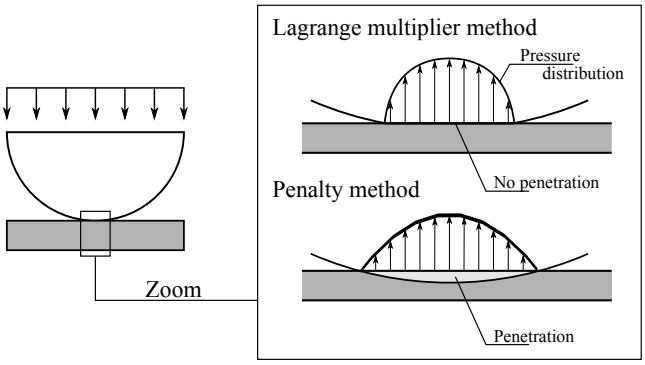

Figure 3: Comparison of Lagrange multiplier and penalty methods on deformation and distribution of contact pressures.

developed in [62]. In this case, the contact constraint is applied in a weak sense over the element. The gap function is computed through the closest-point projection of a point of the non-mortar surface onto the mortar one which is given more importance. It is extrapolated over the element by the means of interpolation functions.

Finally, the *contact domain* discretisation does not involve any projection method [63, 64]. The gap between the solids potentially in contact is discretised by a fictitious mesh. Thence the gap function is continuous between them and avoids many discrepancies and loss of unicity due to projection.

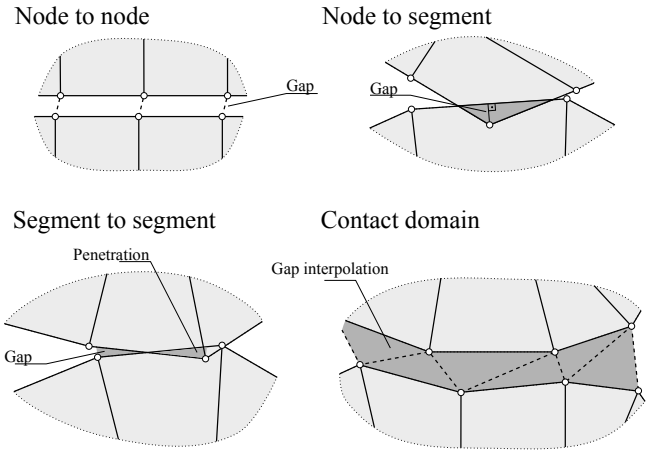

Figure 4: Comparison between the discretisation methods of the contact area.

If the interface represents a discontinuity saturated with a fluid, several additional ingredients are necessary:

- a technique to discretise the flow within and through the interface;

- a law relating the flow to the gradient of pressure.

The *single node* discretisation of flow is the simplest one as shown Figure 5. It simply superposes a discontinuity for fluid flow to a continuous porous medium [65]. In this case, there is no hydro-mechanical coupling and the opening of the discontinuity is constant and user-defined. It acts such as a pipe creating a preferential path for fluid flow.

The *double-node* discretisation describes the fluid flow within the interface as a function of the gradients of pressure of each side of the interface [44, 16, 66, 67]. There is an hydro-mechanical coupling since the discontinuity is able to open. The flow through the interface depends on a transversal transmissivity and the gradient of pressure across the interface.

Another option is to discretise the field of fluid pressure inside the interface by additional nodes. This method is termed *triple-node* discretisation [16, 48]. The underlying hypothesis is that the field of pressure is homogeneous inside the interface. However there is a drop of pressure across the interface, between the two solids in contact.

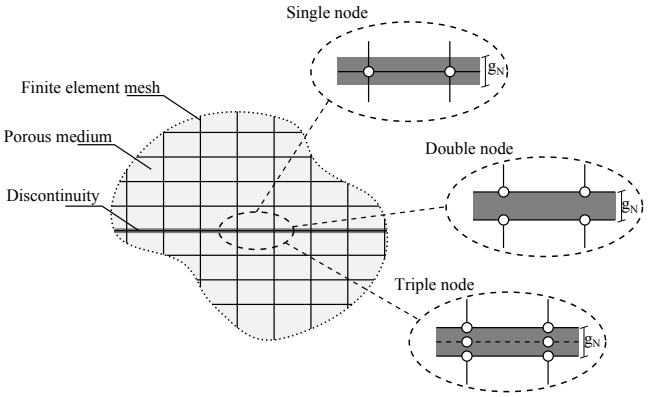

Figure 5: Comparison between the discretisation methods of the flow within and through the interface.

Boussinesq [68] firstly provides a mathematical law characterising the laminar flow of a viscous incompressible fluid between two smooth parallel plates. The total fluid flow is proven to be proportional to the cube of the aperture between the plates, and this relation is termed *cubic law*. In this case, the longitudinal permeability of the fault is a function of its opening g_N

$$k_l = \frac{(g_N)^2}{12}. \tag{1}$$

Its applicability to rock mechanics is proven [69, 43, 70] despite improvements are necessary due to the underlying strong hypothesis. The non smoothness of the rock edges of the interface is taken into account by considering an hydraulic aperture rather than a mechanical one [42].

3. Governing equations of the interface problem

The developed finite element of interface is zero-thickness which is more suitable for large displacements. It does not involve any remeshing technique. The contact constraint is enforced by a penalty method. Indeed, this approach is easy to implement and additional unknowns are not required. Furthermore, the implementation is based on an analogy with elastoplasticity. It is very flexible and complex constitutive laws can be introduced instead. The fluid flow within and across the interface is discretised using a three-node approach taking easily into account the storage and longitudinal flow.

3.1. Mechanical problem

3.1.1. Definition of the mechanical problem and gap function

Let us consider two deformable porous media Ω^1 and Ω^2 in their current configurations at time t. The global system of coordinates is termed $(\mathrm{E}_1, \mathrm{E}_2, \mathrm{E}_3)$. A 2D cross section of these bodies is illustrated in Figure 6. Their evolution is assumed to be quasi-static. Their boundaries in current configurations are denoted Γ^1 and Γ^2. Imposed displacement (Dirichlet) and traction(Neumann) boundaries are respectively denoted $\Gamma^i_{\bar{u}}$ and $\Gamma^i_{\bar{t}}$.
Γ^1_c and Γ^2_c denote both parts of the boundary where contact is likely to happen. In that area, a local system of coordinate $(\mathbf{e}^1_1, \mathbf{e}^1_2, \mathbf{e}^1_3)$ is defined along the mortar side Γ^1_c as shown in Figure 6, where $\mathbf{e}^1_1$ denotes the normal to the surface. The closest point projection $\bar{\mathbf{x}}^1$ of a point of $\mathbf{x}^2$ of the boundary Γ^2_c onto Γ^1_c is defined such that [54]

$$\mathrm{g}_N = \left(\mathbf{x}^2 - \bar{\mathbf{x}}^1\right) \cdot \bar{\mathbf{e}}^1_1, \tag{2}$$

where $(\bar{\mathbf{e}}^1_1, \bar{\mathbf{e}}^1_2, \bar{\mathbf{e}}^1_3)$ denotes the local system of coordinates at point $\bar{\mathbf{x}}^1$. This function g_N is referred as the gap function, where the subscript N stands for normal direction. If there is no contact between the solids, g_N is positive. The contact is termed *ideal* if there is no interpenetration of the solids. For instance in Hertzian contact [71], the gap function is equal to zero. This can be enforced if the Lagrange multiplier method is used. If the penalty method is employed, interpenetration is necessary to generate contact pressure and the gap function becomes negative.

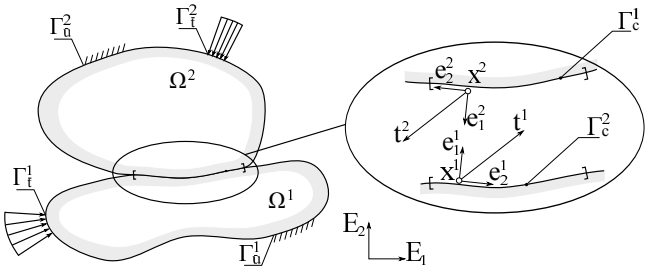

Figure 6: Statement of the mechanical problem, cross-section of the 3D problem in the $(\mathrm{E}_1, \mathrm{E}_2)$ plane.

The definition of a relative tangential displacement between two points in the plane of contact has no meaning in the field of large displacement [33]. Instead normal (N) and tangential ($T1$ and $T2$) velocities are defined in the local system of coordinates. They are gathered into the vector $\dot{\mathbf{g}}$ such that

$$\dot{\mathbf{g}} = \dot{g}_N \, \mathbf{e}_1^1 + \dot{g}_{T1} \, \mathbf{e}_2^1 + \dot{g}_{T2} \, \mathbf{e}_3^1. \tag{3}$$

3.1.2. Normal contact constraint

Contact between two solids gives birth to non-zero stress vectors $\mathbf{t}^1 = -\mathbf{t}^2$ along their common boundary as shown in Figure 6. These vectors are described in the corresponding local system of coordinates at each contacting point such that

$$\mathbf{t}^1 = -\mathrm{p}_N \, \mathbf{e}_1^1 + \tau_1 \, \mathbf{e}_2^1 + \tau_2 \, \mathbf{e}_3^1, \tag{4}$$

where p_N is the normal pressure, τ_1 and τ_2 are the shear stresses in both directions in the plane of the interface. The ideal contact constraint is summarised into the Hertz-Signorini-Moreau condition [54],

$$\mathrm{g}_N \geq 0, \qquad \mathrm{p}_N \geq 0 \qquad \text{and} \qquad \mathrm{p}_N \, \mathrm{g}_N = 0. \tag{5}$$

If there is no contact, the gap function g_N is positive and the contact pressure p_N is null. When contact arises, the gap function is null and the contact pressure is positive.

This condition is not verified any more if the penalty method is used. In case of contact, the relation between the pressure and the gap function reads

$$\dot{\mathrm{p}}_N = -\mathrm{K}_N \, \dot{\mathrm{g}}_N, \tag{6}$$

where the minus sign ensures the contact pressure is positive when interpenetration increases, i.e. $\mathrm{g}_N < 0$ and $\dot{\mathrm{g}}_N < 0$.

3.1.3. Tangential contact constraint

When solids are in contact, the ideal tangential behaviour of the interface distinguishes between the *stick* and *slip* states [54]. In the former state, two points in contact cannot move tangentially. They keep stuck together during the simulation, *i.e.* $\dot{\mathrm{g}}_{T1} = 0$ and $\dot{\mathrm{g}}_{T2} = 0$. The second state involves a relative tangential displacement in the plane of the interface. This is summarised in a condition similar to Eq. (5)

$$\dot{\mathrm{g}}_{Ti}^{sl} \geq 0, \qquad f(\mathbf{t}, \mathbf{q}) \leq 0 \qquad \text{and} \qquad \dot{\mathrm{g}}_{Ti}^{sl} \, f(\mathbf{t}, \mathbf{q}) = 0 \qquad\qquad i = 1, 2 \tag{7}$$

where $\dot{\mathrm{g}}_{Ti}^{sl}$ is the variation of the non-recoverable displacement in each tangential direction. It is related to the variation of tangential displacement

$$\dot{\mathbf{g}}_T = \mathrm{sign}(\dot{\tau}_1) \, \dot{\mathrm{g}}_{T1}^{sl} \, \mathbf{e}_2^1 + \mathrm{sign}(\dot{\tau}_2) \, \dot{\mathrm{g}}_{T2}^{sl} \, \mathbf{e}_3^1. \tag{8}$$

Stick and *slip* states are distinguished by the criterion $f(\mathbf{t}, \mathbf{q})$. It depends on the stress state $\mathbf{t}$ and a set of internal variables $\mathbf{q}$. The evolution of the stress state within the interface depends on the constitutive law described hereafter.

The ideal *stick* state, $\dot{\mathbf{g}}_T = 0$, is also regularised by the penalty method, *i.e.* a relative displacement is allowed. Thence the relation between the shear stress and the tangential variation of displacement reads

$$\dot{\tau}_i = \mathrm{K}_T \, \dot{\mathrm{g}}_{Ti} \qquad i = 1, 2. \tag{9}$$

3.1.4. Constitutive law

It is shown that both rock joints and soil-structure interfaces present a very complex mechanical behaviour [72, 73, 74, 58] inducing dilatancy, degradation of the friction angle, critical state... This paper focuses on the general formulation of the coupled finite element of interface. Therefore the constitutive law is kept as basic as possible in order to highlight the coupling inherent to the formulation. The Mohr-Coulomb criterion is adopted for that purpose. However interested reader should refer to [75, 39, 41] for a deeper insight into more accurate constitutive laws.

The constitutive law adopted only depends on the stress state $\mathbf{t}$ within the interface and a single internal variable, the friction coefficient μ. Mathematically it reads

$$f(\mathbf{t}, \mu) = \underbrace{\sqrt{(\tau_1)^2 + (\tau_2)^2}}_{\|\tau\|} - \mu \, \mathrm{p}_N. \tag{10}$$

where $\|\tau\|$ is the norm of the tangential stresses. The criterion is represented in Figure 7b. In the absence of contact, the stress state lies on the apex of the criterion. Both normal pressure and tangential stresses are null, *i.e.* $\mathbf{t} = \mathbf{0}$. If the combination of tangential and normal stresses lies below the criterion ($f < 0$), the tangential state is considered *stick*. Otherwise, if the stress state lies on the criterion ($f = 0$), the tangential state is considered as *slip*.

	No contact	Stick	Slip
p_N	$= 0$	> 0	> 0
$\|\tau\|$	$= 0$	≥ 0	$= \mu \cdot p_N$

(a) Stress state in the interface in each case.

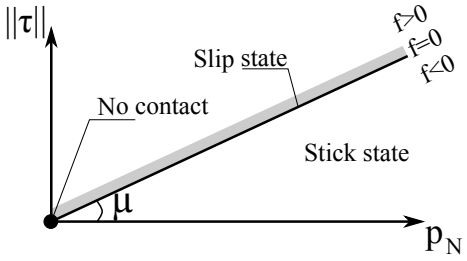

(b) Mohr-Coulomb criterion.

Figure 7: Differentiation of stick and slip states through the Mohr-coulomb criterion.

The evolution of the stresses lies within the framework of elastoplasticity. Indeed the *stick* state is regularised and can be compared to an elastic state. Therefore the incremental relation between variations of stresses $\dot{\mathbf{t}}$ and variations

of the gap function $\dot{\mathbf{g}}$ reads

$$\begin{bmatrix} \dot{\mathrm{p}}_N \\ \dot{\tau}_1 \\ \dot{\tau}_2 \end{bmatrix} = \underbrace{\begin{bmatrix} -K_N & 0 & 0 \\ 0 & \mathrm{K}_T & 0 \\ 0 & 0 & \mathrm{K}_T \end{bmatrix}}_{\mathbf{D}^e} \cdot \begin{bmatrix} \dot{\mathrm{g}}_N \\ \dot{\mathrm{g}}_{T,1} \\ \dot{\mathrm{g}}_{T,2} \end{bmatrix}, \tag{11}$$

where $\mathbf{D}^e$ is equivalent to the elastic compliance tensor. In this case, the penalty coefficients introduced on a purely numerical basis are compared to elastic coefficients which are physical. When the interface reaches the slip state, an elastoplastic compliance tensor $\mathbf{D}^{ep}$ is defined such that

$$\begin{bmatrix} \dot{\mathrm{p}}_N \\ \dot{\tau}_1 \\ \dot{\tau}_2 \end{bmatrix} = \underbrace{\begin{bmatrix} -K_N & 0 & 0 \\ -\mu\,\mathrm{K}_N\,\dfrac{\tau_1}{\|\tau\|} & \mathrm{K}_T\left(1-\dfrac{(\tau_1)^2}{\|\tau\|^2}\right) & -\mathrm{K}_T\,\dfrac{\tau_1\,\tau_2}{\|\tau\|^2} \\ -\mu\,\mathrm{K}_N\,\dfrac{\tau_2}{\|\tau\|} & -\mathrm{K}_T\,\dfrac{\tau_1\,\tau_2}{\|\tau\|^2} & \mathrm{K}_T\left(1-\dfrac{(\tau_2)^2}{\|\tau\|^2}\right) \end{bmatrix}}_{\mathbf{D}^{ep}} \cdot \begin{bmatrix} \dot{\mathrm{g}}_N \\ \dot{\mathrm{g}}_{T,1} \\ \dot{\mathrm{g}}_{T,2} \end{bmatrix}. \tag{12}$$

This tensor is introduced in [31] and is based on a non-associated flow rule.

3.1.5. Continuum formulation

Each solid Ω^i verifies the classic mechanical equilibrium equations in quasi-static conditions [76]. Solving the mechanical contact problem consists in finding the field of displacement $\mathbf{u}$ for all points $\mathbf{x} \in \Omega^i$ verifying these equations and subjected to the contact constraints Eqs. (5) and (7).
Considering a field of admissible virtual velocities $\delta\dot{\mathbf{x}}$ on Ω^i, the weak form of the principle of virtual power reads

$$\sum_{i=1}^{2}\left[\int_{\Omega^i}\boldsymbol{\sigma} : \boldsymbol{\epsilon}\left(\delta\dot{\mathbf{x}}\right)\,\mathrm{d}\Omega\right] = \sum_{i=1}^{2}\left[\int_{\Omega^i}\bar{\mathbf{f}} : \delta\dot{\mathbf{x}}\,\mathrm{d}\Omega + \int_{\Gamma^i_{\bar{\mathbf{t}}}}\bar{\mathbf{t}} : \delta\dot{\mathbf{x}}\,\mathrm{d}\Omega + \int_{\Gamma^i_c}\mathbf{T}^i : \delta\dot{\mathbf{x}}\,\mathrm{d}\Gamma\right], \tag{13}$$

where $\bar{\mathbf{f}}$ are the body forces, $\bar{\mathbf{u}}$ are the imposed displacements, $\bar{\mathbf{t}}$ are the imposed tractions, $\mathbf{n}$ is the normal to $\Gamma^i_{\bar{\mathbf{t}}}$ and $\mathbf{T}^i$ is the projection of the local stress tensor $\mathbf{t}^i$ in global coordinates. The equality of Eq. (13) is enforced when the contact area Γ^i_c is known.

3.2. Flow problem

3.2.1. Definition of the problem

Let us consider a discontinuity of very thin width embedded in a porous medium in its current configuration, as depicted in Figure 8. This could represent for example an open fault within a rock mass. This discontinuity creates a preferential path for fluid flow. Moreover there is a transversal fluid flow between the rock mass and the discontinuity.

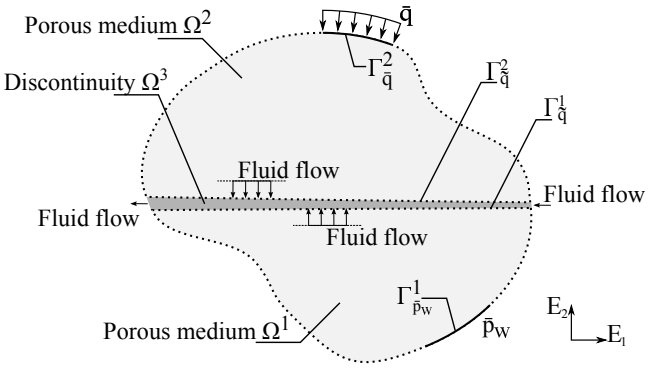

Figure 8: Definition of the flow problem (cross section of the 3D case in the (E_1, E_2) plane), porous medium, discontinuity and boundaries.

There is a conceptual difference between the treatment of the mechanical and flow contact problems. The mechanical contact constraint consists of a non-zero pressure p_N applied along the contact zone Γ_c between the two solids Ω^1 and Ω^2.

On the other hand, the opening of the discontinuity creates a gap g_N filled with water. This gap creates a new volume Ω^3 in which fluid flow takes place, as shown in Figure 9. It is bounded by the two porous media Ω^1 and Ω^2. Their boundary are termed $\Gamma^1_{\tilde{q}}$ and $\Gamma^2_{\tilde{q}}$. Therefore $\Gamma_{\tilde{q}}$ represents a boundary where the solids are close enough, fluid interaction hold and mechanical contact is likely to happen. It always includes the contact zone Γ_c.

Ω^3 is modelled as an equivalent porous medium. The fluid flow within it is described by the cubic law. Fluid flows exist between the inner volume Ω^3 and both adjacent porous media Ω^1 and Ω^2. This flow is a function of the difference of pressure between them. This is a non-classical boundary condition since it is not a imposed flux nor an imposed pressure.

Finally imposed flux and pressure boundaries on Ω^1 and Ω^2 are respectively denoted $\Gamma^i_{\bar{q}}$ and $\Gamma^i_{\bar{p}_w}$.

3.2.2. Fluid flow formulation

A three-node formulation is adopted to describe the fluid flow through and within the interface, as described in Figure 10. Therefore fluid pressures on each side of the interface (p_{w1} and p_{w2}) and inner fluid pressure (p_{w3}) are the fluid variables. At each point within the interface, four fluxes are defined

- two longitudinal fluxes (f_{wl1} and f_{wl2}) in the local tangential directions $(\mathbf{e}^1_2, \mathbf{e}^1_3)$ in the plane of the interface;
- two transversal fluxes (f_{wt1} and f_{wt2}) in the local normal direction $(\mathbf{e}^1_1)$.

The generalised Darcy's law is assumed to reproduce the local longitudinal fluid flows f_{wl1} and f_{wl2} in the plane of the interface. It reads in each local

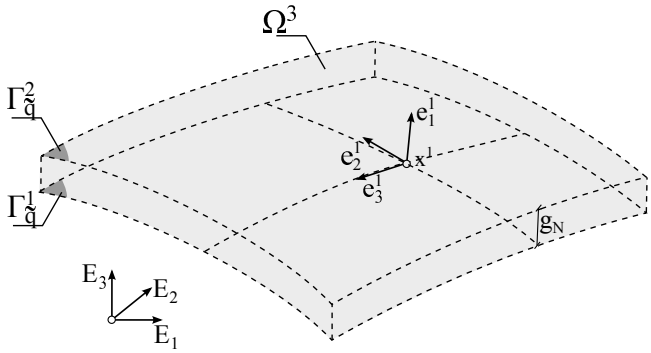

Figure 9: Definition of the equivalent interior porous medium Ω^3 bounded by $\Gamma^1_{\tilde{q}}$ and $\Gamma^2_{\tilde{q}}$.

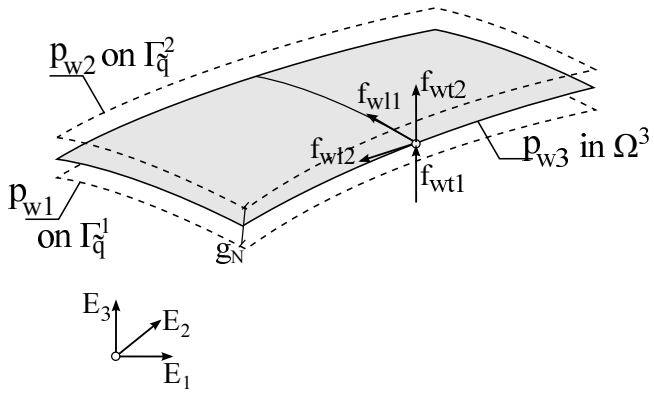

Figure 10: Definition of longitudinal and transversal flows.

tangential direction $(\mathbf{e}^1_2, \mathbf{e}^1_3)$,

$$\mathrm{f}_{wl(i-1)} = -\frac{k_l}{\mu_w}\left(\nabla_{\mathbf{e}^1_i}\,\mathrm{p}_{w3} + \rho_w\,\mathrm{g}\,\nabla_{\mathbf{e}^1_i} z\right)\rho_w \qquad \text{for} \quad i = 2,3 \tag{14}$$

where $\nabla_{\mathbf{e}^1_i}$ is the gradient in the direction $\mathbf{e}^1_i$, μ_w is the dynamic viscosity of the fluid, g the acceleration of gravity, ρ_w is the density of the fluid and k_l is the permeability.

Each transversal fluid flux is a function of a transversal conductivity T_{wi} and the drop of pressure across $\Gamma^i_{\tilde{q}}$. They read

$$\mathrm{f}_{wt1} = \rho_w\,\mathrm{T}_{w1}\,(\mathrm{p}_{w1} - \mathrm{p}_{w3}) \qquad \text{on} \quad \Gamma^1_{\tilde{q}}, \tag{15}$$

$$\mathrm{f}_{wt2} = \rho_w\,\mathrm{T}_{w2}\,(\mathrm{p}_{w3} - \mathrm{p}_{w2}) \qquad \text{on} \quad \Gamma^2_{\tilde{q}}. \tag{16}$$

3.2.3. Continuum formulation

Each porous medium Ω^i i=, 1, 2, 3 verifies the classic hydraulic equilibrium equations [77]. Solving the contact problem consists in finding the pore water

distribution on Ω^i verifying the equilibrium equations and satisfying the non-classical boundary conditions Eqs. (15)-(16) over $\Gamma^i_{\tilde{\mathrm{q}}}$. Considering a field of admissible virtual pore water pressures $\delta \mathrm{p}_w$ on Ω, the weak formulation of the virtual power principle reads

$$\sum_{i=1}^{3} \left[\int_{\Omega^i} \dot{\mathrm{S}}\, \delta \mathrm{p}_w - \mathbf{f}_w \cdot \boldsymbol{\nabla} \left(\delta \mathrm{p}_w \right) \, \mathrm{d}\Omega \right] = \sum_{i=1}^{3} \left[\int_{\Omega^i} \bar{\mathrm{Q}}\, \delta \mathrm{p}_w \, \mathrm{d}\Omega + \int_{\Gamma^i_{\bar{\mathrm{q}}}} \bar{\mathrm{q}}\, \delta \mathrm{p}_w \, \mathrm{d}\Gamma + \int_{\Gamma^i_{\tilde{q}}} \tilde{\mathrm{q}}\, \delta \mathrm{p}_w \, \mathrm{d}\Gamma \right] \tag{17}$$

where $\mathbf{f}_w$ is the fluid flux at point $\mathbf{x}$, $\dot{\mathrm{S}}$ is the storage term, $\bar{\mathrm{Q}}$ is the imposed volume source, $\bar{\mathrm{p}}_w$ is the imposed fluid pressure, $i = 1, 2$ corresponds to the two porous media in contact and $i = 3$ to the volume of the interface. The fluid flow $\tilde{\mathrm{q}}$ along the boundary corresponds to the transversal fluid flows f_{wti} defined in Eqs. (15) and (16). The source term $\bar{\mathrm{Q}}$ associated to Ω^3 is null.
The mechanical problem was given more importance to the mortar side Γ^1_c. Similarly, the integral over Ω^3 is transformed into a surface integral over $\Gamma^1_{\tilde{\mathrm{q}}}$. This hypothesis is valid since it is assumed the inner pressure is constant over the aperture g_N of the interface. Thence, Eq. (17) for $i = 3$ finally reads

$$\int_{\Gamma^1_{\tilde{\mathrm{q}}}} \left[\dot{\mathrm{S}}\, \delta \mathrm{p}_w - \mathrm{f}_{wl1}\, \nabla_{\mathbf{e}^1_2} \left(\delta \mathrm{p}_w \right) - \mathrm{f}_{wl2}\, \nabla_{\mathbf{e}^1_3} \left(\delta \mathrm{p}_w \right) \right] \mathrm{g}_N \, \mathrm{d}\Gamma = \int_{\Gamma^1_{\tilde{\mathrm{q}}}} \rho_w\, \mathrm{T}_{w1}\, \left(\mathrm{p}_{w1} - \mathrm{p}_{w3} \right) \delta \mathrm{p}_w - \rho_w\, \mathrm{T}_{w2}\, \left(\mathrm{p}_{w3} - \mathrm{p}_{w2} \right) \delta \mathrm{p}_w \, \mathrm{d}\Gamma, \tag{18}$$

where $\nabla_{\mathbf{e}^1_i}$ is the gradient in the $\mathbf{e}^1_i$ direction.

In the porous media Ω^1 and Ω^2, the storage component $\dot{\mathrm{S}}$ is coupled with the deformation of the solid skeleton. The treatment of this component for Ω^3 is different and treated hereafter.

3.3. Couplings between mechanical and flow problems

The flow problem within the interface intrinsically depends on the mechanical problem. The gap function g_N defined in the mechanical problem directly influences total fluid flow within the interface since the cubic law is related to the mechanical opening g_N.
However, it is worth noting hydraulic and mechanical apertures should sometimes be differentiated. If two perfectly smooth plates are in ideal contact, the gap function g_N is equal to zero between them. Thence the fluid flow is null since the permeability is equal to zero. However, if the surfaces are rough, a fluid flow is still possible even if the solids are in contact. A residual hydraulic aperture D_0 is considered. Hence, the permeability is computed according to

[42, 16]

$$k_l = \begin{cases} \dfrac{(\mathrm{D}_0)^2}{12} & \text{if} \quad \mathrm{g}_N \leq 0 \\ \dfrac{(\mathrm{D}_0 + \mathrm{g}_N)^2}{12} & \text{otherwise.} \end{cases} \tag{19}$$

It is updated during the simulation to take into account the possible gap aperture.

A second coupling is created by the storage component $\dot{\mathrm{S}}$. The variation of the total mass of fluid $\dot{\mathrm{M}}_f$ stored in Ω^3 comes respectively from the variation of the fluid density, the opening/closing of the gap and the variation of the surface of the discontinuity, namely

$$\dot{\mathrm{M}}_f \quad = \quad \underbrace{\left(\dot{\rho}_w \, \mathrm{g}_N + \rho_w \, \dot{\mathrm{g}}_N + \rho_w \, \mathrm{g}_n \, \frac{\dot{\Gamma}_{\tilde{q}}}{\Gamma_{\tilde{q}}} \right)}_{\dot{\mathrm{S}}} \Gamma_{\tilde{q}}. \tag{20}$$

where $\dot{\mathrm{S}}$ is the storage term of Eq. (17). In the following, the fluid is assumed incompressible $\dot{\rho}_w = 0$ and only the geometrical storage is taken into account. In many applications, the main component of the storage is due to the opening/closing of the interface $\dot{\mathrm{g}}_N$.

The mechanical behaviour of the interface also depends on the fluid flow within it. Indeed, the total pressure p_N acting on each side $\Gamma^i_{\tilde{q}}$ of the interface is defined according to the Terzaghi's principle [78]. It is decomposed into an effective mechanical pressure p'_N and a fluid pressure equal to the inner pressure p_{w3},

$$\mathrm{p}_N = \mathrm{p}'_N + \mathrm{p}_{w3}. \tag{21}$$

In this case, all the developments applied to the mechanical contact constraint and constitutive laws in Sections 3.1.2 and 3.1.4 must be treated with reference to the effective pressure p'_N rather than to the total pressure p_N.

4. Numerical formulation of an interface finite element

The discretisation of the governing equations is based on a segment to segment approach. It is suitable for large relative displacements. Fluid flows are discretised according to the triple-node approach. This method allows the modelling of a drop of pressure across the interface. The inner nodes discretising a field of pressure make possible the modelling of an interface between two distinct media, for instance a soil and a foundation.

4.1. Space and fluid pressure discretisation

The presented coupled interface finite element are isoparametric and quadrangular [79]. A complete representation of the interface requires twelve nodes, as shown in Figure 11:

- nodes 1,2,3,4 : first side of the interface $\Gamma^1_{\tilde{q}}$, three mechanical (coordinates x,y,z) and a pore water pressure (p_w) degrees of freedom per node;
- nodes 5,6,7,8 : inner nodes of the interface Ω^3, a pore water pressure (p_w) degree of freedom per node;
- nodes 9,10,11,12 : second side of the interface $\Gamma^2_{\tilde{q}}$, three mechanical (coordinates x,y,z) and a pore water pressure (p_w) degrees of freedom per node.

Mechanical and hydraulic degrees of freedom are gathered into the vector of generalised coordinates at each node i such that

$$\mathbf{u}^i = \left[\mathrm{x^i}, \mathrm{u^i}, \mathrm{z^i}, \mathrm{p}^i_w\right]^T \qquad i = 1,2,3,4,9,10,11,12 \tag{22}$$

$$\mathrm{u}^i = \left[\mathrm{p}^i_w\right] \qquad i = 5,6,7,8. \tag{23}$$

These coordinates are continuously interpolated over the element using classic linear interpolation functions $\phi^i(\xi,\eta)$ related to each node i of the side interpolated. Continuous generalised velocities $\dot{\mathbf{u}}$ are interpolated over the element accordingly from nodal values $\dot{\mathbf{u}}^i$.

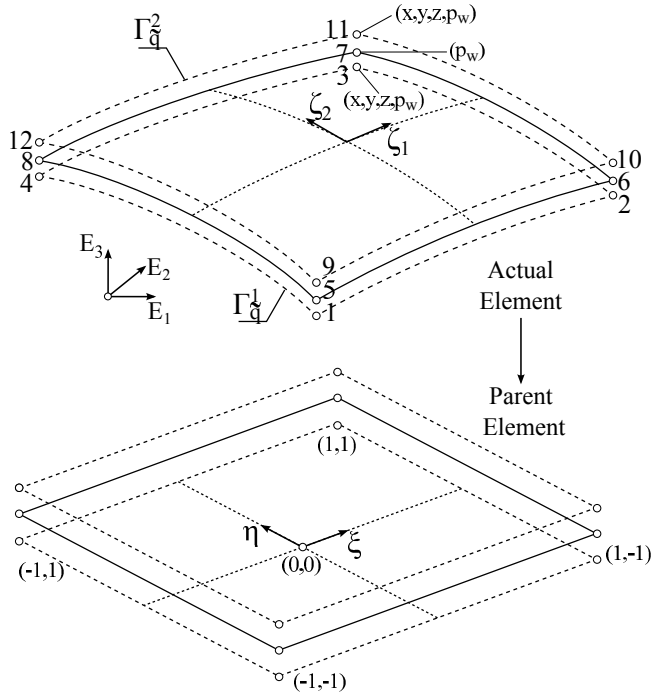

Figure 11: Discretisation of the interface into isoparametric elements from convective ($\zeta_1\zeta_2$) to local coordinates (ξ,η). Transformation to the parent element.

4.2. Mechanical problem

4.2.1. Local system of coordinates and gap function

The first step of the mechanical formulation is the determination of the local system of coordinates. The rotation matrix $\mathbf{R}$ relates the global $(\mathrm{E}_1, \mathrm{E}_2, \mathrm{E}_3)$ to the local $(\mathrm{e}_1^1, \mathrm{e}_2^1, \mathrm{e}1_3)$ system of coordinates. This rotation matrix is computed with respect to the side $\Gamma_{\tilde{q}}^1$, which is the mortar side. Let us first consider the components in global axes of two unit non-orthogonal vectors respectively parallel to each edge of an element, namely

$$\mathbf{e}_\xi = \frac{1}{\sqrt{\left(\frac{\partial \mathrm{x}}{\partial \xi}\right)^2 + \left(\frac{\partial \mathrm{y}}{\partial \xi}\right)^2 + \left(\frac{\partial \mathrm{z}}{\partial \xi}\right)^2}} \left[\frac{\partial \mathrm{x}}{\partial \xi}, \quad \frac{\partial \mathrm{y}}{\partial \xi}, \quad \frac{\partial \mathrm{z}}{\partial \xi}\right]^T, \tag{24}$$

$$\mathbf{e}_\eta = \frac{1}{\sqrt{\left(\frac{\partial \mathrm{x}}{\partial \eta}\right)^2 + \left(\frac{\partial \mathrm{y}}{\partial \eta}\right)^2 + \left(\frac{\partial \mathrm{z}}{\partial \eta}\right)^2}} \left[\frac{\partial \mathrm{x}}{\partial \eta}, \quad \frac{\partial \mathrm{y}}{\partial \eta}, \quad \frac{\partial \mathrm{z}}{\partial \eta}\right]^T. \tag{25}$$

The normal to the element is given by the cross product,

$$\mathbf{e}_1^1 = \mathbf{e}_\xi \times \mathbf{e}_\eta. \tag{26}$$

The first tangential direction $\mathbf{e}_2^1$ is identical to $\mathbf{e}_\xi$ and the second tangential direction is their cross product

$$\mathbf{e}_3^1 = \mathbf{e}_1^1 \times \mathbf{e}_2^1. \tag{27}$$

Thence the rotation matrix is the assembling of these vectors

$$\mathbf{R} = \begin{bmatrix} \mathbf{e}_1^1 & \mathbf{e}_2^1 & \mathbf{e}_3^1 \end{bmatrix}. \tag{28}$$

According to the continuous Eq.(2), the gap function at each point of $\Gamma_{\tilde{q}}^e$ is computed according to

$$\dot{\mathbf{g}} = \begin{bmatrix} \dot{\mathrm{g}}_N \\ \dot{\mathrm{g}}_{T,1} \\ \dot{\mathrm{g}}_{T,1} \end{bmatrix} = [\mathbf{R}]^T \cdot \begin{bmatrix} \dot{\mathrm{x}}_2 - \dot{\mathrm{x}}_1 \\ \dot{\mathrm{y}}_2 - \dot{\mathrm{y}}_1 \\ \dot{\mathrm{z}}_2 - \dot{\mathrm{z}}_1 \end{bmatrix} = [\mathbf{R}]^T \cdot \Delta\dot{\mathbf{x}}. \tag{29}$$

where the subscript indicates either the side 1 or side 2 of the interface. The norm of the Jacobian of the transformation of the element from the convective system of coordinates (ζ_1, ζ_2) to the isoparametric system (ξ, η) reads

$$\|\mathbf{J}\| = \sqrt{\left(\frac{\partial \mathrm{x}}{\partial \xi}\right)^2 + \left(\frac{\partial \mathrm{y}}{\partial \xi}\right)^2 + \left(\frac{\partial \mathrm{z}}{\partial \xi}\right)^2} \sqrt{\left(\frac{\partial \mathrm{x}}{\partial \eta}\right)^2 + \left(\frac{\partial \mathrm{y}}{\partial \eta}\right)^2 + \left(\frac{\partial \mathrm{z}}{\partial \eta}\right)^2}. \tag{30}$$

The full definition of the rotation matrix and its derivatives are available in Appendix A.

4.2.2. External energetically equivalent nodal forces

The mechanical contribution of a single interface element to the external virtual power expression is derived from the continuous Eq. (13). The energetically equivalent nodal forces associated to node i of the interface element are computed numerically using a Gauss-scheme. For instance, the mechanical nodal forces acting on the boundary of Ω^1 are computed according to

$$\mathbf{F}_E^i = \sum_{IP=1}^{n_{IP}} \left[\mathbf{R}\cdot\mathbf{t}\,\phi^i\,\|\mathbf{J}\|\,\mathrm{W}\right]_{IP}, \tag{31}$$

where ϕ^i is the interpolation function associated to node i and the expression between brackets is evaluated in each of the n_{IP} integration points, associated to the Gauss weight W. Reaction forces acting on Ω^2 are computed accordingly. The full derivation of all energetically equivalent nodal forces is provided in Appendix B.

4.3. Flow problem

4.3.1. Internal energetically equivalent nodal forces

Fluid flow inside the equivalent porous medium Ω^3, along the interface, involves energetically equivalent internal forces. This component is derived from Eq. (18). It is numerically computed according to

$$\mathrm{F}_I^i = \sum_{IP=1}^{n_{IP}} \left[\left(\dot{\mathrm{S}}\,\phi^i - \mathrm{f}_{wl1}\,\nabla_{\mathbf{e}_2^1}\left(\phi^i\right) - \mathrm{f}_{wl2}\,\nabla_{\mathbf{e}_3^1}\left(\phi^i\right)\right)\,\|\mathbf{J}\|\,\mathrm{g}_N\,\mathrm{W}\right]_{IP}. \tag{32}$$

4.3.2. External energetically equivalent nodal forces

Transversal fluid flows between Ω^1, Ω^2 and Ω^3 provides energetically equivalent external nodal forces related to fluid degrees of freedom. The contribution to the external virtual power corresponding to Ω^3 is derived from Eq. (18). For instance, it is numerically computed on the boundary of Ω^1 according to

$$\mathrm{F}_E^i = \sum_{IP=1}^{n_{IP}} \left[\left(\rho_w\,\mathrm{T}_{w1}\,\left(\mathrm{p}_{w1}-\mathrm{p}_{w3}\right)\,\phi^i - \rho_w\,\mathrm{T}_{w2}\,\left(\mathrm{p}_{w3}-\mathrm{p}_{w2}\right)\,\phi^i\right)\,\|\mathbf{J}\|\,\mathrm{W}\right]_{IP}, \tag{33}$$

where p_{w1} is the fluid pressure on side 1, p_{w2} on side 2 and p_{w3} inside. The reaction forces acting on the boundary of Ω^2 are computed similarly.

4.4. Time discretisation

Internal $\mathbf{F}_I^i$ and external $\mathbf{F}_E^i$ nodal forces defined in Eqs. (31), (32) and (33) are gathered into the global vectors $\mathbf{F}_I$ and $\mathbf{F}_E$. Thence vector of out of balance forces $\mathbf{F}_{OB}$ is defined according to

$$\mathbf{F}_{OB} = \mathbf{F}_I - \mathbf{F}_E. \tag{34}$$

The fluid flow problem within a porous medium is inherently time dependent. Therefore, modelling its evolution requires the discretisation of time. It

is assumed the media in contact are initially in equilibrium at a given time t, *i.e.* $\mathbf{F}_{OB} = \mathbf{0}$. The equilibrium of the discretised system should be verified over a whole time step Δt such that

$$\int_t^{t+\Delta t} \mathrm{G}(t)\, \mathbf{F}_{OB}\, \mathrm{d}t = \mathbf{0} \tag{35}$$

where $\mathrm{G}(t)$ is a weighting function. In this work, the weighting function is reduced to a collocation $\delta(\theta)$, where δ is the Dirac function. It is proven that a choice of $\theta \geq 0.5$ leads to an unconditionally stable time scheme [79]. In this work, the integration scheme is implicit, i.e. $\theta = 1$. The equilibrium is then written at the end of the time step.

4.5. Stiffness matrix

The stiffness matrix $\mathbf{K}$ related to the interface element is computed analytically by derivation of out of balance forces related to node i with respect do generalised degree of freedom j. The extended developments are provided in Appendix C

5. Extraction of a suction caisson

5.1. Statement of the problem

A suction caisson made of steel is assumed embedded in an elastic soil as shown in Figure 12a. The vertical loading of this caisson is detailed in the following. Despite the problem is fundamentally 2D, a quarter of the caisson is modelled in 3D in order to validate the formulation of the interface element. The geometric parameters defining the problem are provided in Table 1.

The caisson is composed of an horizontal lid at the top and a vertical skirt, as depicted in Figure 12b. The ratio of the skirt thickness to diameter is greater than actual caissons [80, 4]. Indeed, the skirt of the caisson is represented by volume element which cannot be too elongated in order to avoid numerical disturbances.

The soil is represented by a quarter of a cylindrical layer. Its radius is equal to 24m and its height to 12m, as shown in Figure 12a. The finite element mesh is composed of 8288 nodes and 6945 elements, including volume, interface and boundary elements. Volume elements are composed of 8 nodes and interpolation functions are linear for both mechanical and pressure degrees of freedom. Four integration points are used over the interface finite elements.

The soil layer is assumed to lie at 10m under the sea level. The two lateral faces are considered undrained because of the symmetry. The others sides are drained since the soil layer is assumed very large with respect to the geometry of the caisson. The loading consists in imposing vertical displacements at the top of the caisson, as shown in Figure 12c.

The mudline delineates the solid and liquid phases at the bottom of the sea. It is assumed a thin layer of poorly compacted soil lies over the solid phase. It is

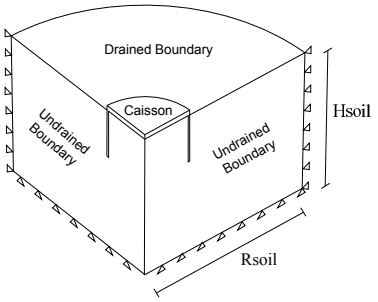

(a) Global sketch of the geometry of the problem.

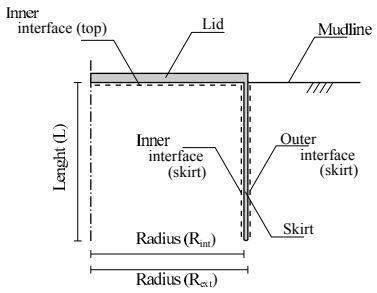

(b) Description of the caisson.

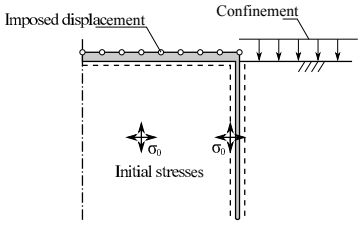

(c) Initial conditions and loading.

Figure 12: Statement of the case study.

not explicitly modelled but represented by a vertical confinement (10 kPa), as represented in Figure 12c.

The caisson is assumed already installed within the soil. Thence effective initial stresses due to the dead weight are set up within the soil layer and the interface. The hydrostatic pore water pressures corresponding to the depth of water are initialised.

Caisson					Soil		Mesh	
R_{int}	R_{ext}	L	t_{skirt}	t_{lid}	R_{soil}	H_{soil}	N_{nodes}	N_{elems}
3.8m	3.9m	4m	0.1m	0.4m	24m	12m	8288	6945

Table 1: Geometrical parameters: R_{int} inner radius, R_{ext} outer radius, L length, t_{skirt} thickness of the skirt, t_{lid} thickness of the lid, R_{soil} outer radius of the soil domain, H_{soil} thickness of the soil layer, N_{nodes} number of nodes, N_{elems} number of elements.

The mechanical behaviour of the soil and the caisson are assumed linear elastic. It is not true at all for the soil as it was previously shown in the literature [5, 13, 14]. However, this work focuses on interface behaviour and additional complexity is avoided. Parameters of the constitutive laws are presented in Table 2. The porosity n and the specific mass γ_s are identical for the soil

and the steel in order to ensure a problem initially in equilibrium. The soil is assumed isotropic, therefore the coefficient of earth pressure at rest K_0 is equal to one. The permeability is equal to 1.E-11m^2.
Transversal conductivity T_w characterising the interface is null between the caisson and the interface (the caisson is impervious) but not null between the soil and the interface. The residual hydraulic aperture is equal to 5.E-5m. Thence there is always a longitudinal fluid flow event in case of contact. The soil caisson friction coefficient is equal to 0.57 corresponding to a friction angle of 30°.

Soil					
E [MPa]	ν [-]	n [-]	k [m^2]	γ_s [kg/m^3]	K_0 [-]
2E2	0.3	0.36	1.E-11	2650	1
Caisson					
E [MPa]	ν [-]	n [-]	k [m^2]	γ_s [kg/m^3]	K_0 [-]
2E5	0.3	0.36	0	2650	1
Interface					
K_N [N/m^3]	K_T [N/m^3]	μ [-]	T_w [m.Pa^{-1}.s^{-1}]	D_0 [m]	
1E10	1E10	0.57	1.E-8	1.E-5	

Table 2: Material parameters: E Young modulus, ν Poisson's ratio, n porosity, k permeability, γ_s density of solid grains, K_0 coefficient of earth pressure at rest, K_N, K_T penalty coefficients, μ friction coefficient, T_w transversal conductivity, D_0 residual hydraulic aperture.

The loading consists in the vertical uplifting of the caisson. Displacement of nodes at its top are imposed as shown in Figure 12c.
Two types of simulations are carried out in order to validate the formulation of the 3D interface element. If the loading rate of the caisson is sufficiently low or the permeability of the soil is very high, over- or underpressures generated within the soil are almost instantaneously dissipated. In this case, the simulation is termed *drained*. This highlights the progressive soil-caisson sliding during the simulation and the purely mechanical behaviour of the problem. There is not transient effects.
In the second kind of simulation, pore pressures generated during loading are able to dissipate progressively within the surrounding soil. It is termed *partially drained* and highlights the hydro-mechanical behaviour of the interface. Purely transient effects are highlighted. Longitudinal and transversal fluid flows hold and can be verified.

5.2. Drained simulation (purely mechanical problem)

During a pull simulation, the total load applied to the top of the caisson is balanced by the weight of the caisson and friction along the skirt as shown in Figure 13. This figure represents the variation of total load ΔF_{tot} with displacement, total friction outside the caisson ΔF_{ext} and total friction inside the caisson ΔF_{int}.

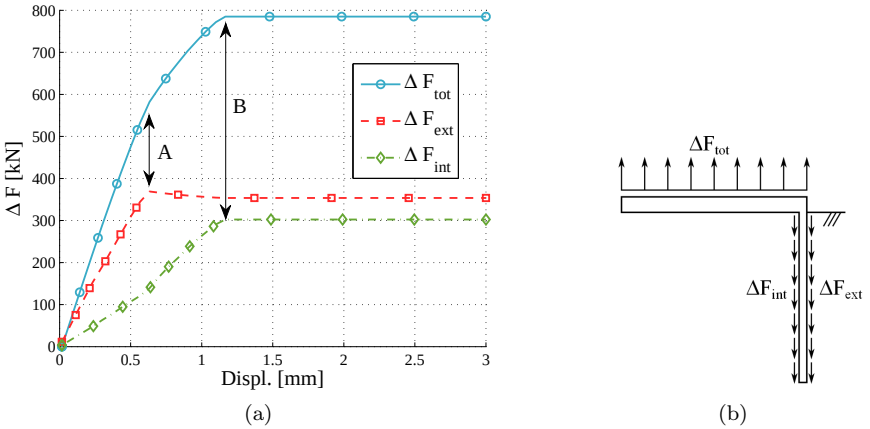

Figure 13: Drained pull simulation of the suction caisson: ΔF_{tot} variation of total vertical load, ΔF_{ext} integral of shear mobilised outside the caisson, ΔF_{int} integral of shear mobilised inside the caisson.

At the early beginning, the variation of ΔF_{ext} and ΔF_{int} is nearly linear, as depicted in Figure 13a. Indeed, the shear stress mobilised within the interface varies according to

$$\dot{\tau} = K_T \, \dot{g}_T \leq \mu \, p'_N. \tag{36}$$

Maximum shear stress τ is bounded by the Mohr criterion. However at the early beginning ($g_T \ll$) the shear stress has not yet reached this criterion and the evolution of τ is linear. The interface is in the *stick state* previously defined. The maximum shear stress increases with depth due to the increasing confinement. Therefore friction is not reached simultaneously over the whole skirt. The reduced shear $\eta_{ext} = (\tau/p'_N)_{ext}$ progressively reaches the friction coefficient μ from the top of the caisson to its tip, as shown in Figure 14. Thence, there is a progressive sliding between the caisson and the surrounding soil, starting from the top, where normal pressure is the lowest.

The diffusion of the shear stress from the vertical interface to the soil induces a stress state tending to separate the soil and the caisson near the surface. A vertical gap between the soil and the caisson is created near the surface as shown in Figure 14. The reduced mobilised shear η_{ext} is equal to zero in this zone, where contact is lost.

Finally, at point A in Figure 13a, the outer friction is fully mobilised along the skirt, thence ΔF_{ext} reaches a plateau and there is a slope breakage in ΔF_{tot}.

Similar conclusions can be drawn when considering the curve ΔF_{int} in Figure 13a. However the caisson confines the soil inside it. Thence the soil tends to be plugged in the caisson as it was already observed in the literature [11]. This reduces the magnitude of relative tangential displacement $\dot{\mathbf{g}}_T$, thence the slope of ΔF_{int} is less steep than ΔF_{ext}. The distribution of reduced shear mobilised is more uniform illustrating this effect, as shown in Figure 15. Consequently a

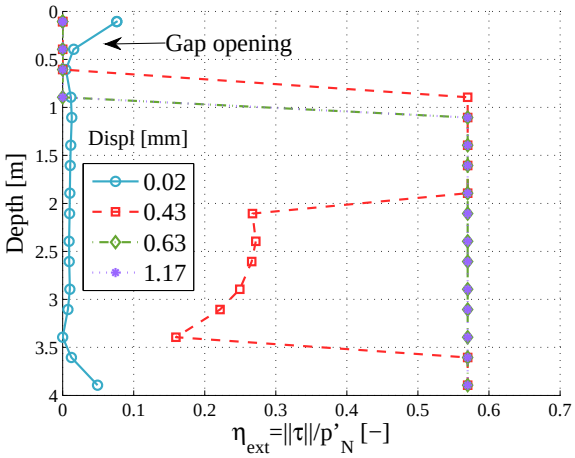

Figure 14: Drained pull simulation of the suction caisson, mobilised shear along the skirt outside the caisson (η_{ext}).

larger displacement is necessary to reach the full mobilisation of friction along the inner skirt and the final plateau described by point B in Figure 13a.

The uplifting displacement can be kept increasing since the interface element is able to represent large displacements. The total load required to pull the caisson progressively decreases because the surface along which friction can be mobilised is progressively reduced, as can be shown in Figure 16.

The step shape of the results is purely numerical. Indeed, the contact constraint is weakly enforced and computed numerically at each integration point. Therefore, while there is a non-mortar element in front of a mortar element, $\Delta F_{tot,1}$ and $\Delta F_{ext,1}$ corresponding to the reference mesh are constant. Each drop of ΔF_{tot} corresponds to a new integration point of the mortar side which is not any more in front of a non mortar side. This tendency can be smoothed by increasing the number of nodes describing the interface or the number of integration points. $\Delta F_{tot,2}$ corresponds to a mesh with a greater number of nodes describing the interface.

5.3. Partially drained simulation (coupled problem)

Figure 17 represents the load-displacement results in case of partially drained simulation. The pull rate of the caisson is equal to v_p =1mm/min. The partially drained behaviour entails a greater load at the beginning of the plateau than the drained behaviour. A new reaction force ΔF_{uw} sustains the pull load. It is obtained by integrating the variation of pressure Δp_w under the lid of the caisson.

This resistance is similar to a suction effect used to install the caisson. Physically, it corresponds to an inverse consolidation process where the total vertical load decreases and the vertical displacement occurs upwards as shown in Figure

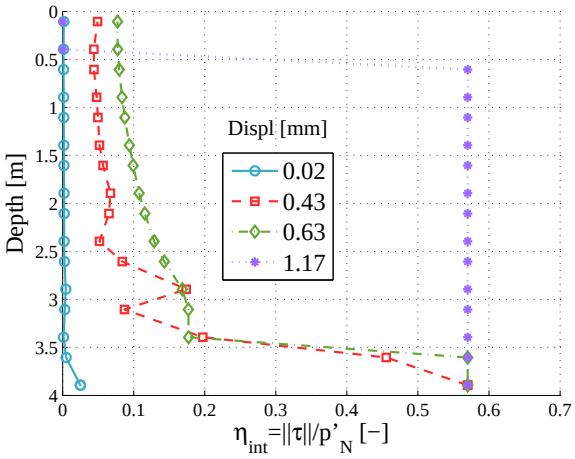

Figure 15: Drained pull simulation of the suction caisson, mobilised shear along the skirt inside the caisson (η_{int}).

19. The fluid pressure decreases accordingly, creating a differential of pressure between inside and outside the caisson, as shown in Figure 18. This creates an incoming fluid flux, progressively reducing the differential of pressure.

The frictional behaviour in Figure 17 is similar to the drained simulation. Points A and B correspond to the full mobilisation of friction along the skirt, respectively outside ΔF_{ext} and inside ΔF_{int} the caisson.

The evolution of ΔF_{pw} increases gently up to point A. During this first phase, the soil plug and the caisson move nearly together, as shown in Figure 19. The displacement Δy_{top} is identical for two nodes at the centre of the caisson, respectively on the soil and on the caisson sides. The consolidation effect is negligible as well as the variation of fluid pressure Δp_w.
From this point, contact is lost between the top soil and the caisson. Thence a gap is created and filled with water. A transversal flux f_t takes places through the interface, as depicted in Figure 19. This total flux is obtained by integrating the transversal fluid flux f_{wt1} over the top surface of the soil. This effect superposes to the consolidation process and increases the inside/outside differential of pressure.
The rate of opening of the gap as well as the transversal fluid flux strongly increase after the full mobilisation of friction inside and outside the caisson, at point B. The suction component of reaction ΔF_{pw} starts increasing significantly accordingly. Finally a stationary phase is established. The inverse settlement of the soil Δy_{top} reaches a plateau as well as the total transversal fluid flux. The transversal fluid flow is equal to the storage rate of fluid within the gap, which is analytically assessed assuming the caisson has a rigid body motion

$$\dot{S} = \rho_w \, \dot{v}_p \, \pi R_{int}^2/4 = 1.89\,10^{-1}\,\mathrm{kg/s} \tag{37}$$

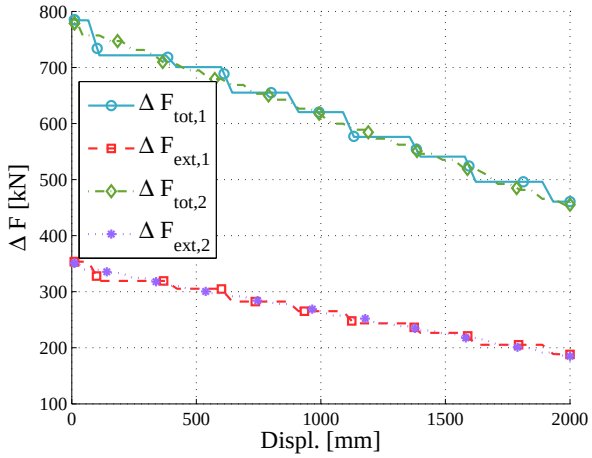

Figure 16: Drained pull simulation of the suction caisson (large displacement). $\Delta F_{tot,1}$ correspond to the reference mesh and $\Delta F_{tot,2}$ to a higher number of nodes.

which is very close to the numerically computed value in Figure 19.

The drained simulation highlights the loss of contact between the skirt of the caisson and the soil, for instance in Figure 14 where $\eta_{ext} = 0$. In the partially drained simulation, this loss of contact creates a preferential path for longitudinal fluid flow along the caisson. Figure 20 depicts this flow and the gap g_N opening along the caisson, at the end of the simulation. The higher the gap, the higher the flow since the permeability is gap dependent.
This gap opening reduces the efficiency of the caisson since it speeds up the dissipation of underpressures inside the caisson. However if elastoplastic constitutive laws are used, the pipe creation is reduced [81]. Indeed in case of cohesionless soils, such a gap is not stable.

6. Conclusion

The role of interfaces is crucial in many fields of geotechnical and geological engineering. They create preferential paths for fluid flow and/or deformations. Therefore the assessment of their behaviour is of crucial importance for engineers.
This paper presents a zero-thickness 3D hydro-mechanical coupled finite element of interface. It is implemented in the finite element code `LAGAMINE` which is able to solve fully coupled problems.
The mechanical contact constraint is enforced by a penalty method and discretised by the mortar method. It is able to reproduce large sliding displacements due to the full mobilisation of friction within the interface. A Mohr-Coulomb criterion is adopted to compute the maximum shear stress available within the interface. It is very flexible since any other constitutive law characterising both

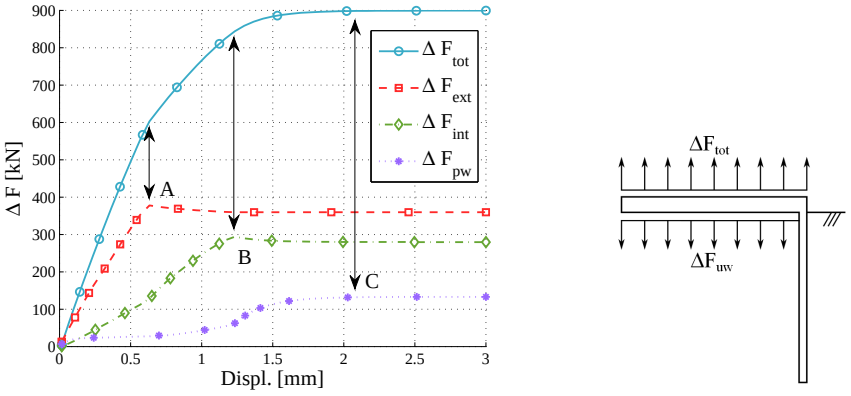

Figure 17: Partially drained pull simulation of the suction caisson: ΔF_{tot} variation of total vertical load, ΔF_{ext} integral of shear mobilised outside the caisson, ΔF_{int} integral of shear mobilised inside the caisson, ΔF_{uw} integral of the variation of water pressure at the top inside the caisson.

the normal and tangential behaviours can be implemented easily.

The fluid problem is discretised by a three-node approach. The unknowns of the fluid problem are the fluid pressures. Their discretisation on each side of the interface and inside it is necessary to compute longitudinal and transversal flows.

The generalised Darcy's law describes the longitudinal fluid flow, discretised on interior nodes. The longitudinal permeability depends on the aperture of the interface (cubic law), introducing a coupling between mechanical and hydraulic behaviours. A second coupling follows from the decomposition of the total pressure acting on each side on the interface into an effective mechanical pressure and a fluid pressure, equal to interior pressure.

The transversal fluid flow is a function of the difference of pressure between each side of the interface and the pressure inside. The flow linearly depends on a user-defined transversal conductivity. This introduces a drop of pressure across the discontinuity.

The interface element is applied and validated on a pull test of a suction caisson embedded in an elastic soil. A drained simulation verifies the purely mechanical behaviour of the interface. The caisson progressively slides out of the soil when the friction is fully mobilised within the interface. A large uplift of the caisson is also reproduced.

The partially drained simulation illustrates the coupling features of the element. The uplift of the caisson creates a gap between it and the soil. This gap is filled with water, creating a drop of fluid pressure and a water flow from outside to inside the caisson across the interface.

The stress distribution around the caisson opens the outside interface between the soil and the caisson. This creates a preferential path for fluid flow along the

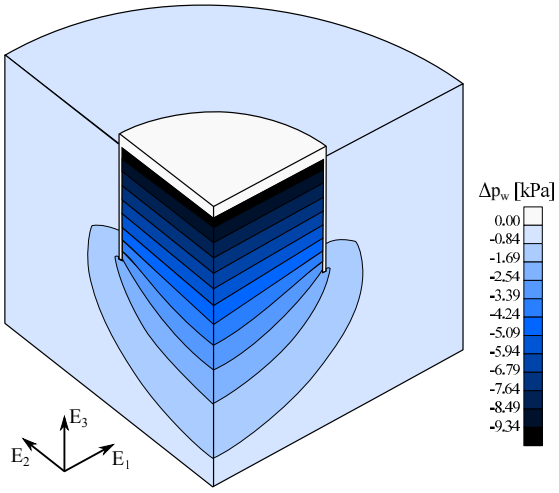

Figure 18: Variations of pore water pressure Δp_w within the soil around the caisson, at the end of the simulation.

skirt, decreasing the suction effect of the caisson.

7. Acknowledgements

The authors would like to acknowledge the F.R.S.-F.N.R.S for its financial support.

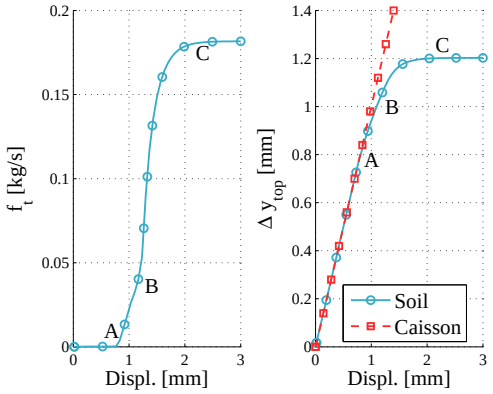

(a) Total transversal flux between the soil and the interface inside the caisson (left); vertical displacement of the top soil inside caisson.

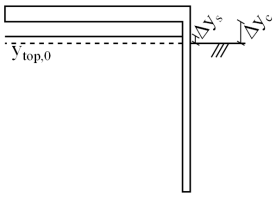

(b) Displacement of the soil Δy_s, displacement of the caisson Δy_c, initial position of soil and caisson $y_{top,0}$.

Figure 19: Partially drained pull simulation of the suction caisson.

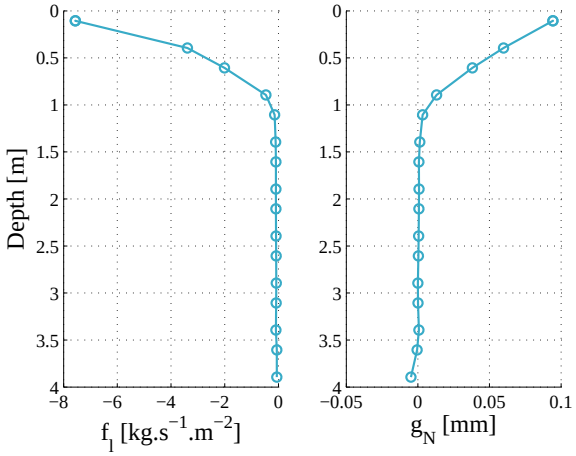

Figure 20: Relation between the longitudinal flux and the opening of a gap along the skirt, outside the caisson, end of the simulation.

References

[1] D. White, B. Lehane, Friction fatigue on displacement piles in sand, Géotechnique 54 (10) (2004) 645–658.

[2] D. Sheng, P. Wriggers, S. Sloan, Improved numerical algorithms for frictional contact in pile penetration analysis, Computers and Geotechnics 33 (6-7) (2006) 341–354.

[3] B. Stuyts, J. Irvine, D. Cathie, Assessing the stability of piled tripod foundations for offshore wind turbines under cyclic loading, in: Proceedings of the 8th International Conference on Structural Dynamics, EUDORYN 2011, Leuven, 2011, pp. 3482–3489.

[4] R. Kelly, G. Houlsby, B. Byrne, A comparison of field and laboratory tests of caisson foundations in sand and clay, Géotechnique 56 (9) (2006) 617–626.

[5] B. Cerfontaine, S. Levasseur, F. Collin, R. Charlier, Axisymmetric transient modelling of a suction caisson in dense sand, in: Numerical Methods in Geotechnical Engineering - Proceedings of the 8th European Conference on Numerical Methods in Geotechnical Engineering, NUMGE 2014, Vol. 2, 2014, pp. 1243–1248.

[6] B. Lehane, S. Elkhatib, S. Terzaghi, Extraction of suction caissons in sand, Géotechnique 64 (9) (2014) 735–739.

[7] M. Iskander, S. El-Gharbawy, R. Olson, Performance of suction caissons in sand and clay, Canadian Geotechnical Journal 584 (may) (2002) 576–584.

[8] G. Houlsby, L. Ibsen, B. Byrne, Suction Caissons for Wind Turbines, International Symposium on Frontiers in Offshore Geotechnics 75 (September) (2005) 94.

[9] L. Andresen, H. Jostad, K. Andersen, Finite Element Analyses Applied in Design of Foundations and Anchors for Offshore Structures, International Journal of Geomechanics 11 (December) (2011) 417–430.

[10] K. Andersen, H. Jostad, R. Dyvik, Penetration resistance of offshore skirted foundations and anchors in dense sand, Journal of Geotechnical and Geoenvironmental Engineering 134 (June 2001) (2008) 106–116.

[11] M. Senders, M. Randolph, CPT-Based method for the installation of suction caissons in sand, Journal of Geotechnical and Geoenvironmental Engineering 135 (January) (2009) 14–25.

[12] F. Villalobos, B. Byrne, G. Houlsby, An experimental study of the drained capacity of suction caisson foundations under monotonic loading for offshore applications, Soils and foundations 49 (3) (2009) 477–488.

[13] K. Thieken, M. Achmus, C. Schröder, On the behavior of suction buckets in sand under tensile loads, Computers and Geotechnics 60 (2014) 88–100.

[14] B. Cerfontaine, F. Collin, R. Charlier, Vertical transient loading of a suction caisson in dense sand, in: Computer Methods and Recent Advances in Geomechanics - Proceedings of the 14th Int. Conference of International Association for Computer Methods and Recent Advances in Geomechanics, IACMAG 2014, 2015, pp. 929–934.

[15] P. Segall, Earthquakes triggered by fluid extraction, Geology 17 (10) (1989) 942–946.

[16] C. Guiducci, A. Pellegrino, J.-P. Radu, F. Collin, R. Charlier, Numerical modeling of hydro-mechanical fracture behavior, in: Numerical models in Geomechanics, 2002, pp. 293–299.

[17] C. Li, P. Bars, L. Laloui, Coupled approach to assess caprock deformation caused by co2 injection, in: Geotechnical Special Publication, 2014, pp. 651–657.

[18] A. Dieudonne, B. Cerfontaine, F. Collin, R. Charlier, Hydromechanical modelling of shaft sealing for co2storage, Engineering Geologydoi:doi:10.1016/j.enggeo.2015.04.016.

[19] J. Rutqvist, J. Birkholzer, C.-F. Tsang, Coupled reservoir–geomechanical analysis of the potential for tensile and shear failure associated with co2 injection in multilayered reservoir–caprock systems, International Journal of Rock Mechanics and Mining Sciences 45 (2) (2008) 132–143.

[20] M. Zoback, S. Gorelick, Earthquake triggering and large-scale geologic storage of carbon dioxide, Proceedings of the National Academy of Sciences 109 (26) (2012) 10164–10168.

[21] R. Goodman, R. Taylor, T. Brekke, A model for the mechanics of jointed rock, Journal of the Soil Mechanics and Foundations Division 94.

[22] A. Curnier, A theory of friction, International Journal of Solids and Structures 20 (7) (1984) 637–647.

[23] G. Beer, An isoparametric joint/interface element for finite element analysis, International Journal for Numerical Methods in Engineering 21 (1985) 585–600.

[24] A. Klarbring, G. Björkman, A mathematical programming approach to contact problems with friction and varying contact surface, Computers & Structures 30 (5) (1988) 1185–1198.

[25] A. Gens, I. Carol, E. Alonso, An interface element formulation for the analysis of soil reinforcement interaction, Computers and Geotechnics 7 (1988) 133–151.

[26] J. Schellekens, R. De Borst, On the numerical integration of interface elements, International Journal for Numerical Methods in Engineering 36 (1) (1993) 43–66.

[27] P. Wriggers, Finite element algorithms for contact problems, Archives of Computational Methods in Engineering 2 (4) (1995) 1–49.

[28] V. Kaliakin, J. Li, Insight into deficiencies associated with commonly used zero-thickness interface elements, Computers and Geotechnics 17 (2) (1995) 225–252.

[29] G. Zavarise, P. Wriggers, B. Schrefler, A method for solving contact problems, International Journal for Numerical Methods in Engineering 42 (3) (1998) 473–498.

[30] P. Wriggers, L. Krstulovic-Opara, J. Korelc, Smooth c1-interpolations for two-dimensional frictional contact problems, International Journal for Numerical Methods in Engineering 51 (12) (2001) 1469–1495.

[31] R. Charlier, S. Cescotto, Modélisation du phénomène de contact unilatéral avec frottement dans un contexte de grandes déformations, Journal de Mécanique Théorique et Appliquée 7 (Suppl. 1).

[32] T. Laursen, J. Simo, A continuum-based finite element formulation for the implicit solution of multibody, large deformation-frictional contact problems, International Journal for Numerical Methods in Engineering 36 (20) (1993) 3451–3485.

[33] A. Habraken, S. Cescotto, Q. Banning, Contact between deformable solids: The fully coupled approach, Mathematical and Computer modelling 28 (4) (1998) 153–169.

[34] J. Ghaboussi, E. Wilson, J. Isenberg, Finite element for rock joints and interfaces, Journal of the Soil Mechanics and Foundations Division 99 (1973) 933–848.

[35] C. Desai, E. C. Drumm, M. Zaman, Cyclic Testing and Modelling of Interfaces, Journal of Geotechnical Engineering - ASCE I (6) (1985) 793–815.

[36] R. Day, D. Potts, Zero thickness interface elements - numerical stability and application, International Journal for Numerical and Analytical Methods in Geomechanics 18 (1994) 689–708.

[37] A. Gens, I. Carol, E. Alonso, A constitutive model for rock joints formulation and numerical implementations, Computers and Geotechnics 9 (1990) 3–20.

[38] M. Boulon, A. Selvadurai, H. Benjelloun, B. Feuga, Influence of rock joint degradation on hydraulic conductivity, International Journal of Rock Mechanics and Mining Sciences 30 (7) (1993) 1311–1317.

[39] G. Mortara, M. Boulon, V. Ghionna, A 2-d constitutive model for cyclic interface behaviour, International journal for numerical and analytical methods in geomechanics 26 (11) (2002) 1071–1096.

[40] H. Liu, E. Song, H. Ling, Constitutive modeling of soil-structure interface through the concept of critical state soil mechanics, Mechanics Research Communications 33 (2006) 515–531. doi:10.1016/j.mechrescom.2006.01.002.

[41] H. Liu, H. Ling, Constitutive description of interface behavior including cyclic loading and particle breakage within the framework of critical state soil mechanics, International Journal for Numerical and Analytical Methods in Geomechanics 32 (January) (2008) 189–213. doi:10.1002/nag.

[42] R. Olsson, N. Barton, An improved model for hydromechanical coupling during shearing of rock joints, International Journal of Rock Mechanics and Mining Sciences 38 (3) (2001) 317–329.

[43] Y. Tsang, P. Witherspoon, Hydromechanical behavior of a deformable rock fracture subject to normal stress, Journal of Geophysical Research: Solid Earth 86 (B10) (1981) 9287–9298.

[44] K. Ng, J. Small, Behavior of joints and interfaces subjected to water pressure, Computers and Geotechnics 20 (1) (1997) 71–93.

[45] J. Segura, I. Carol, On zero-thickness interface elements for diffusion problems, International journal for numerical and analytical methods in geomechanics 28 (9) (2004) 947–962.

[46] R. Juanes, J. Samper, J. Molinero, A general and efficient formulation of fractures and boundary conditions in the finite element method, International Journal for Numerical Methods in Engineering 54 (12) (2002) 1751–1774.

[47] M. Ferronato, G. Gambolati, C. Janna, P. Teatini, Numerical modelling of regional faults in land subsidence prediction above gas/oil reservoirs, International journal for numerical and analytical methods in geomechanics 32 (6) (2008) 633–657.

[48] B. Jha, R. Juanes, Coupled multiphase flow and poromechanics: A computational model of pore pressure effects on fault slip and earthquake triggering, Water Resources Research 50 (2014) 3376–3808.

[49] F. Collin, Y. Cui, C. Schroeder, R. Charlier, Mechanical behaviour of lixhe chalk partly saturated by oil and water: experiment and modelling, International journal for numerical and analytical methods in geomechanics 26 (9) (2002) 897–924.

[50] P. Gerard, R. Charlier, R. Chambon, F. Collin, Influence of evaporation and seepage on the convergence of a ventilated cavity, Water resources research 44 (5). doi:doi:10.1029/2007WR0065.

[51] K. Sharma, C. Desai, Analysis and implementation of thin-layer element for interfaces and joints, Journal of Engineering Mechanics 118 (27005) (1993) 2442–2462.

[52] X. Wang, L. Wang, Continuous interface elements subject to large shear deformations, International Journal of Geomechanics 6 (April) (2006) 97–107.

[53] P. Wriggers, J. Schröder, A. Schwarz, A finite element method for contact using a third medium, Computational Mechanics 52 (4) (2013) 837–847.

[54] P. Wriggers, Computational contact mechanics, 2nd Edition, Wiley : Chichester, 2006.

[55] P. Wriggers, G. Zavarise, Encyclopedia of Computational Mechanics, Vol. 2: Solids and Structures, 2004, Ch. 6: Computational Contact Mechanics.

[56] D. Luenberger, Y. Ye, Linear and nonlinear programming, 3rd Edition, Vol. 116, Springer, 2008.

[57] E. Alonso, M. Zandarín, S. Olivella, Joints in unsaturated rocks: Thermo-hydro-mechanical formulation and constitutive behaviour, Journal of Rock Mechanics and Geotechnical Engineering 5 (3) (2013) 200–213.

[58] M. Zandarin, E. Alonso, S. Olivella, A constitutive law for rock joints considering the effects of suction and roughness on strength parameters, International Journal of Rock Mechanics and Mining Sciences 60 (2013) 333–344.

[59] J. Hallquist, G. Goudreau, D. Benson, Sliding interfaces with contact-impact in large-scale lagrangian computations, Computer Methods in Applied Mechanics and Engineering 51 (1) (1985) 107–137.

[60] M. Puso, T. Laursen, A mortar segment-to-segment contact method for large deformation solid mechanics, Computer Methods in Applied Mechanics and Engineering 193 (6) (2004) 601–629.

[61] K. Fischer, P. Wriggers, Mortar based frictional contact formulation for higher order interpolations using the moving friction cone, Computer methods in applied mechanics and engineering 195 (37) (2006) 5020–5036.

[62] F. Belgacem, P. Hild, P. Laborde, The mortar finite element method for contact problems, Mathematical and Computer Modelling 28 (4) (1998) 263–271.

[63] J. Oliver, S. Hartmann, J. Cante, R. Weyler, J. Hernández, A contact domain method for large deformation frictional contact problems. part 1: theoretical basis, Computer Methods in Applied Mechanics and Engineering 198 (33) (2009) 2591–2606.

[64] S. Hartmann, J. Oliver, R. Weyler, J. Cante, J. Hernández, A contact domain method for large deformation frictional contact problems. part 2: numerical aspects, Computer Methods in Applied Mechanics and Engineering 198 (33) (2009) 2607–2631.

[65] B. Berkowitz, J. Bear, C. Braester, Continuum models for contaminant transport in fractured porous formations, Water Resources Research 24 (8) (1988) 1225–1236.

[66] J. Segura, I. Carol, Coupled hm analysis using zero-thickness interface elements with double nodes. part i: Theoretical model, International Journal for Numerical and Analytical Methods in Geomechanics 32 (18) (2008) 2083–2101.

[67] J. Segura, I. Carol, Coupled hm analysis using zero-thickness interface elements with double nodes. part ii: Verification and application, International Journal for Numerical and Analytical Methods in Geomechanics 32 (18) (2008) 2103–2123.

[68] J. Boussinesq, Mémoire sur l'influence des frottements dans les mouvements réguliers des fluides, Journal de Mathématiques Pures et Appliquées.

[69] P. Witherspoon, J. Wang, K. Iwai, J. Gale, Validity of cubic law for fluid flow in a deformable rock fracture, Water Resources Research 16 (6) (1980) 1016–1024.

[70] A. Oron, B. Berkowitz, Flow in rock fractures: The local cubic law assumption reexamined, Water Resources Research 34 (11) (1998) 2811–2825.

[71] H. Hertz, Ueber die Berührung fester elastischer Körper, Journal für die reine und angewandte Mathematik 92 (1881) 156–171.

[72] L. Hu, J. Pu, Testing and Modeling of Soil-Structure Interface, Journal of Geotechnical and Geoenvironmental Engineering 130 (8) (2004) 851–860. doi:10.1061/(ASCE)1090-0241(2004)130:8(851).

[73] J. DeJong, D. White, M. Randoph, Microscale observation and modeling of soil structure interface behavior using particle image velocimetry, Soils and Foundations 46 (1) (2006) 15–28.

[74] T. Ho, R. Jardine, N. Anh-Minh, Large-displacement interface shear between steel and granular media, Géotechnique 61 (3) (2011) 221–234. doi:10.1680/geot.8.P.086.

[75] I. Shahrour, F. Rezaie, An elastoplastic constitutive relation for the soil-structure interface under cyclic loading, Computers and Geotechnics 21 (1) (1997) 21–39. doi:10.1016/S0266-352X(97)00001-3.

[76] R. Borja, Plasticity : Modeling & Computation, 2013.

[77] R. Lewis, B. Schrefler, The finite element method in the static and dynamic deformation and consolidation of porous media, John Wiley, 1998.

[78] K. Terzaghi, Erdbaumechanik auf Bodenphysikalischer Grundlage (Soil Mechanics based on Soil Physics), 1925.

[79] O. C. Zienkiewicz, R. L. Taylor, Finite Element Method: Volume 1, Fifth Edition, Butterworth-Heinemann, 2000.

[80] B. Byrne, G. Houlsby, Experimental investigations of response of suction caissons to transient vertical loading, Journal of the Geotechnical and Geoenvironmental Engineering 128 (11) (2002) 926–939.

[81] B. Cerfontaine, The cyclic behaviour of sand, from the prevost model to offshore geotechnics, Ph.D. thesis, University of Liege (2014).

Appendix A. Rotation matrix

The rotation matrix $\mathbf{R}$ is provided in indicial notation in order to simplify the mathematical expressions. The expression of each column R_{i1}, R_{i2} and R_{i3} respectively reads

$$\mathrm{R_{i1}} = \epsilon_{kli} \frac{\partial \mathrm{x}_k}{\partial \xi} \frac{\partial \mathrm{x}_l}{\partial \eta} \Bigg/ \left(\sqrt{\frac{\partial \mathrm{x}_j}{\partial \xi} \frac{\partial \mathrm{x}_j}{\partial \xi}} \sqrt{\frac{\partial \mathrm{x}_h}{\partial \eta} \frac{\partial \mathrm{x}_h}{\partial \eta}} \right) \qquad i = 1, 2, 3 \quad \text{(A.1)}$$

$$\mathrm{R_{i2}} = \frac{\partial \mathrm{x}_i}{\partial \xi} \Bigg/ \sqrt{\frac{\partial \mathrm{x}_j}{\partial \xi} \frac{\partial \mathrm{x}_j}{\partial \xi}} \qquad i = 1, 2, 3 \quad \text{(A.2)}$$

$$\mathrm{R_{i3}} = \epsilon_{kli}\, \mathrm{R}_{k1}\, \mathrm{R}_{l2} \qquad i = 1, 2, 3 \quad \text{(A.3)}$$

where mechanical node coordinate x_i of a given point denotes respectively x,y and z if i is equal to 1,2 and 3. This coordinate is respectively interpolated over the element according to

$$\mathrm{x}_i = \phi^N\, \mathrm{x}_i^N \qquad N = 1, 2, 3, 4, \quad \text{(A.4)}$$

where x_i^N is the coordinate in the i direction of the Nth node of the interface element. The derivative with respect to ξ reads[2]

$$\frac{\partial \mathrm{x}_i}{\partial \xi} = \frac{\partial \phi^N}{\partial \xi}\, \mathrm{x}_i^N \qquad N = 1, 2, 3, 4. \quad \text{(A.5)}$$

[2] N is the summation indice.

The derivative with respect to η is computed accordingly. Notation ϵ^{ijk} is the Levi-Civita symbol such that

$$\begin{array}{rcrl} \epsilon_{ijk} & = & 1 & \text{if } (i,j,k) \text{ is } (1,2,3),(3,1,2) \text{ or } (2,3,1), \\ \epsilon_{ijk} & = & -1 & \text{if } (i,j,k) \text{ is } (3,2,1),(1,3,2) \text{ or } (2,1,3), \\ \epsilon_{ijk} & = & 0 & \text{otherwise.} \end{array}$$

The Jacobian of the transformation $\|\mathbf{J}\|$ from the interface element to its isoparametric parent is equal to

$$\|\mathbf{J}\| = \sqrt{\frac{\partial \mathrm{x}_i}{\partial \xi}\,\frac{\partial \mathrm{x}_i}{\partial \xi}}\,\sqrt{\frac{\partial \mathrm{x}_j}{\partial \eta}\,\frac{\partial \mathrm{x}_j}{\partial \eta}}. \tag{A.6}$$

The large displacement component of the stiffness matrix is obtained from the derivation of $\mathbf{R}$ with respect to each coordinate i of the node N, *i.e.* x_i^N. The derivative of the Jacobian of the transformation $\|\mathbf{J}\|$ gives

$$\begin{aligned} \frac{\partial \|\mathbf{J}\|}{\partial \mathrm{x}_k^N} &= \frac{\partial}{\partial \mathrm{x}_k^N}\left[\sqrt{\frac{\partial \mathrm{x}_i}{\partial \xi}\,\frac{\partial \mathrm{x}_i}{\partial \xi}}\,\sqrt{\frac{\partial \mathrm{x}_j}{\partial \eta}\,\frac{\partial \mathrm{x}_j}{\partial \eta}}\right] \qquad i,k=1,2,3 \\ &= \frac{\sqrt{\dfrac{\partial \mathrm{x}_j}{\partial \eta}\,\dfrac{\partial \mathrm{x}_j}{\partial \eta}}}{\sqrt{\dfrac{\partial \mathrm{x}_i}{\partial \xi}\,\dfrac{\partial \mathrm{x}_i}{\partial \xi}}}\,\frac{\partial \phi^N}{\partial \xi}\,\frac{\partial \mathrm{x}_k}{\partial \xi} + \frac{\sqrt{\dfrac{\partial \mathrm{x}_i}{\partial \xi}\,\dfrac{\partial \mathrm{x}_i}{\partial \xi}}}{\sqrt{\dfrac{\partial \mathrm{x}_j}{\partial \eta}\,\dfrac{\partial \mathrm{x}_j}{\partial \eta}}}\,\frac{\partial \phi^N}{\partial \eta}\,\frac{\partial \mathrm{x}_k}{\partial \eta}. \end{aligned} \tag{A.7}$$

The derivative of the first column of the matrix, R_{i1}, reads

$$\begin{aligned} \frac{\partial \mathrm{R}_{i1}}{\partial \mathrm{x}_k^N} &= \frac{\partial}{\partial \mathrm{x}_k^N}\left[\epsilon_{mni}\,\frac{\partial \mathrm{x}_m}{\partial \xi}\,\frac{\partial \mathrm{x}_n}{\partial \eta}\,\frac{1}{\|\mathbf{J}\|}\right] \qquad i,k=1,2,3 \\ &= \epsilon_{mni}\left[\frac{1}{\|\mathbf{J}\|}\,\frac{\partial \phi^N}{\partial \xi}\,\frac{\partial \mathrm{x}_n}{\partial \eta}\,\delta_{mk} + \frac{1}{\|\mathbf{J}\|}\,\frac{\partial \mathrm{x}_m}{\partial \xi}\,\frac{\partial \phi^N}{\partial \eta}\,\delta_{nk} - \frac{\partial \mathrm{x}_m}{\partial \xi}\,\frac{\partial \mathrm{x}_n}{\partial \eta}\,\frac{1}{\|\mathbf{J}\|^2}\,\frac{\partial \|\mathbf{J}\|}{\partial \mathrm{x}_k^N}\right]. \end{aligned} \tag{A.8}$$

The derivative of the second column of the matrix, R_{i2}, reads

$$\begin{aligned} \frac{\partial \mathrm{R}_{i2}}{\partial \mathrm{x}_k^N} &= \frac{\partial}{\partial \mathrm{x}_k^N}\left[\frac{\partial \mathrm{x}_i}{\partial \xi}\Bigg/\sqrt{\frac{\partial \mathrm{x}_l}{\partial \xi}\,\frac{\partial \mathrm{x}_l}{\partial \xi}}\right] \qquad i,k=1,2,3 \\ &= \frac{\partial \phi^N}{\partial \xi}\,\delta_{ik}\Bigg/\sqrt{\frac{\partial \mathrm{x}_l}{\partial \xi}\,\frac{\partial \mathrm{x}_l}{\partial \xi}} - \frac{\partial \mathrm{x}_i}{\partial \xi}\,\frac{\partial \phi^N}{\partial \xi}\,\frac{\partial \mathrm{x}_k}{\partial \xi}\Bigg/\left(\frac{\partial \mathrm{x}_l}{\partial \xi}\,\frac{\partial \mathrm{x}_l}{\partial \xi}\right)^{3/2}. \end{aligned} \tag{A.9}$$

The derivative of the third column of the matrix, R_{i3}, reads

$$\begin{aligned} \frac{\partial \mathrm{R}_{i3}}{\partial \mathrm{x}_k^N} &= \frac{\partial}{\partial \mathrm{x}_k^N}\left[\epsilon_{mni}\,\mathrm{R}_{m1}\,\mathrm{R}_{n2}\right] \qquad i,k=1,2,3 \\ &= \epsilon_{mni}\left[\frac{\partial \mathrm{R}_{m1}}{\partial \mathrm{x}_k^N}\,\mathrm{R}_{n2} + \mathrm{R}_{m1}\,\frac{\partial \mathrm{R}_{n2}}{\partial \mathrm{x}_k^N}\right]. \end{aligned} \tag{A.10}$$

Appendix B. Energetically equivalent nodal forces

Appendix B.1. Structure of the force vector

The finite element of interface is made of 12 nodes and 36 degrees of freedom. The vector of generalised coordinates related to the element $\Gamma_{\tilde{q}}^e$ reads

$$\begin{aligned}\mathbf{u}^{\Gamma_{\tilde{q}}^e} &= \big[[\mathbf{X}^1]^T, \mathrm{p}_w^1, [\mathbf{X}^2]^T, \mathrm{p}_w^2, [\mathbf{X}^3]^T, \mathrm{p}_w^3, [\mathbf{X}^4]^T, \mathrm{p}_w^4, \mathrm{p}_w^5, \mathrm{p}_w^6, \mathrm{p}_w^7, \mathrm{p}_w^8, \\ &\qquad [\mathbf{X}^9]^T, \mathrm{p}_w^9, [\mathbf{X}^{10}]^T, \mathrm{p}_w^{10}, [\mathbf{X}^{11}]^T, \mathrm{p}_w^{11}, [\mathbf{X}^{12}]^T, \mathrm{p}_w^{12}\big]^T \end{aligned} \tag{B.1}$$

where $\big[\mathbf{X}^i\big]^T = [\mathrm{x}^i, \mathrm{y}^i, \mathrm{z}^i]$ gathers the mechanical degrees of freedom related to node i.

The vector of out of balance forces $\mathbf{F}_{OB}$ is computed according to Eq. (34). Its structure is identical to the vector of generalised degrees of freedom $\mathbf{u}$,

$$\begin{aligned}\mathbf{F}_{OB}^{\Gamma_{\tilde{q}}^e} &= \big[[\mathbf{F}_{OBm}^1]^T, \mathrm{F}_{OBf}^1, [\mathbf{F}_{OBm}^2]^T, \mathrm{F}_{OBf}^2, [\mathbf{F}_{OBm}^3]^T, \mathrm{F}_{OBf}^3, [\mathbf{F}_{OBm}^4]^T, \mathrm{F}_{OBf}^4, \\ &\qquad \mathrm{F}_{OBf}^5, \mathrm{F}_{OBf}^6, \mathrm{F}_{OBf}^7, \mathrm{F}_{OBf}^8, [\mathbf{F}_{OBm}^9]^T, \mathrm{F}_{OBf}^9, [\mathbf{F}_{OBm}^{10}]^T, \mathrm{F}_{OBf}^{10}, \\ &\qquad [\mathbf{F}_{OBm}^{11}]^T, \mathrm{F}_{OBf}^{11}, [\mathbf{F}_{OBm}^{12}]^T, \mathrm{F}_{OBf}^{12}\big]^T \end{aligned} \tag{B.2}$$

where $\mathbf{F}_{OBm}^i$ is the vector of mechanical forces at node i and F_{OBf}^i the equivalent fluid forces. It reduces to equivalent fluid forces only for inner nodes ($i = 5, 6, 7, 8$).

Appendix B.2. Mechanical forces

The mechanical components of the nodal forces are computed in Eq. (31). Thence on the first side of the interface Γ_c^1, corresponding to $i = 1, 2, 3, 4$,

$$\mathbf{F}_{OBm}^i = -\sum_{IP=1}^{n_{IP}} \big[\mathbf{R}\cdot\mathbf{t}\,\phi^i\,\|\mathbf{J}\|\,\mathrm{W}\big]_{IP}\,. \tag{B.3}$$

On the other side Γ_c^2, the force vector corresponding to $i = 9, 10, 11, 12$ reads

$$\mathbf{F}_{OBm}^i = \sum_{IP=1}^{n_{IP}} \big[\mathbf{R}\cdot\mathbf{t}\,\phi^i\,\|\mathbf{J}\|\,\mathrm{W}\big]_{IP}\,. \tag{B.4}$$

It must be pointed out that the Jacobian an rotation matrix as well are computed with respect to the mortar side, *i.e.* $\Gamma_{\tilde{q}}^1$, in both cases.

Appendix B.3. Hydraulic forces

The hydraulic components of the nodal forces are computed in Eqs. (32) and (33). On the first side of the interface $\Gamma_{\tilde{\mathrm{q}}}^1$, the hydraulic force related to nodes $i = 1, 2, 3, 4$ reads

$$\mathrm{F}_{OBf}^i = \sum_{IP=1}^{n_{IP}} \big[\rho_w\,\mathrm{T}_{w1}\,(\mathrm{p}_{w1} - \mathrm{p}_{w3})\,\phi^i\,\|\mathbf{J}\|\,\mathrm{W}\big]_{IP}\,. \tag{B.5}$$

On the second side $\Gamma^2_{\tilde{q}}$, this force related to nodes $i = 9, 10, 11, 12$ is computed according to

$$\mathrm{F}^i_{OBf} = -\sum_{IP=1}^{n_{IP}} \left[\rho_w \, \mathrm{T}_{w2} \left(\mathrm{p}_{w3} - \mathrm{p}_{w2}\right) \, \phi^i \, \|\mathbf{J}\| \, \mathrm{W}\right]_{IP} . \tag{B.6}$$

Finally, hydraulic forces related to nodes $i = 5, 6, 7, 8$, taking into account external and internal components read

$$\begin{aligned} \mathrm{F}^i_{OBf} \;=\; & \sum_{IP=1}^{n_{IP}} \left[\left(\dot{\mathrm{S}} \, \phi^i - \mathrm{f}_{wl1} \, \nabla_{\mathbf{e}^1_2} \left(\phi^i\right) - \mathrm{f}_{wl2} \, \nabla_{\mathbf{e}^1_3} \left(\phi^i\right)\right) \, \|\mathbf{J}\| \, \mathrm{g}_N \, \mathrm{W}\right]_{IP} \\ & - \sum_{IP=1}^{n_{IP}} \left[\left(\rho_w \, \mathrm{T}_{w1} \, \left(p_{w1} - \mathrm{p}_{w3}\right) \, \phi^i - \rho_w \, \mathrm{T}_{w2} \, \left(p_{w3} - \mathrm{p}_{w2}\right) \, \phi^i\right) \, \|\mathbf{J}\| \, \mathrm{W}\right]_{IP} . \end{aligned} \tag{B.7}$$

Appendix C. Stiffness matrix

Appendix C.1. Global stiffness matrix

Each term of the stiffness matrix is computed according to

$$[\mathbf{K}]_{ij} = -\frac{\partial}{\partial \mathbf{u}^j} \left(\mathbf{F}^i_I - \mathbf{F}^i_E\right) , \tag{C.1}$$

which is the derivative of the vector of out of balance nodal forces at node i with respect to the vector of generalised degrees of freedom at node j. It is analytically computed in the following. The stiffness matrix corresponding to the element has the following structure

$$\mathbf{K}_{36\times 36} = \begin{bmatrix} [\mathbf{K}]^{\Gamma^1_{\tilde{q}}\Gamma^1_{\tilde{q}}}_{16\times 16} & [\mathbf{K}]^{\Gamma^1_{\tilde{q}}\Omega^3}_{16\times 4} & [\mathbf{K}]^{\Gamma^1_{\tilde{q}}\Gamma^2_{\tilde{q}}}_{16\times 16} \\ [\mathbf{K}]^{\Omega^3\Gamma^1_{\tilde{q}}}_{4\times 16} & [\mathbf{K}]^{\Omega^3\Omega^3}_{4\times 4} & [\mathbf{K}]^{\Omega^3\Gamma^2_{\tilde{q}}}_{4\times 16} \\ [\mathbf{K}]^{\Gamma^2_{\tilde{q}}\Gamma^1_{\tilde{q}}}_{16\times 16} & [\mathbf{K}]^{\Gamma^2_{\tilde{q}}\Omega^3}_{16\times 4} & [\mathbf{K}]^{\Gamma^2_{\tilde{q}}\Gamma^2_{\tilde{q}}}_{16\times 16} \end{bmatrix} , \tag{C.2}$$

where the subscripts provide the size of the submatrix. The first superscript indicates the origin of the nodal force and the second the derivative.

Appendix C.2. Component $[\mathbf{K}]^{\Gamma^1_{\tilde{q}}\Gamma^1_{\tilde{q}}}_{16\times 16}$ *,* i*=* $1, 4$*,* j*=* $1, 4$

Mechanical component

$$\frac{\partial}{\partial \mathbf{x}^j} \mathbf{F}^i_{OBm} \;=\; -\sum_{IP=1}^{n_{IP}} \left[\frac{\partial}{\partial \mathbf{x}^j} \left(\|\mathbf{J}\| \, \mathbf{R}\right) \cdot \mathbf{t} \, \phi^i \, \mathrm{W} + \mathbf{R} \cdot \frac{\partial \, \mathbf{t}}{\partial \mathbf{x}^j} \, \|\mathbf{J}\| \, \phi^i \, \mathrm{W}\right]_{IP} \tag{C.3}$$

and

$$\frac{\partial \mathbf{t}}{\partial \mathbf{x}^j} \;=\; \mathbf{D}^{ep} \cdot \left(\left[\frac{\partial \mathbf{R}}{\partial \mathbf{x}^j}\right]^T \cdot \Delta \dot{\mathbf{x}} - [\mathbf{R}]^T \cdot \boldsymbol{\delta} \, \phi^j\right) . \tag{C.4}$$

Fluid component

$$\frac{\partial}{\partial \mathrm{p}_{w1}^{j}} \mathbf{F}_{OBf}^{i} \;=\; \sum_{IP=1}^{n_{IP}} \left[\rho_w \, \mathrm{T}_{w1} \, \phi^j \, \phi^i \, \|\mathbf{J}\| \, \mathrm{W}\right]_{IP}. \tag{C.5}$$

Coupling components

$$\frac{\partial}{\partial \mathbf{x}^{j}} \mathbf{F}_{OBf}^{i} \;=\; \sum_{IP=1}^{n_{IP}} \left[\rho_w \, \mathrm{T}_{w1} \, (\mathrm{p}_{w1} - \mathrm{p}_{w3}) \, \phi^i \, \frac{\partial}{\partial \mathbf{x}^{j}} \|\mathbf{J}\| \, \mathrm{W}\right]_{IP}. \tag{C.6}$$

Appendix C.3. Component $[\mathbf{K}]_{16\times 4}^{\Gamma_{\tilde{q}}^{1}\Omega^{3}}$ *,* $i = 1, 4$*,* $j = 5, 8$

Coupling component

$$\frac{\partial}{\partial \mathrm{p}_{w3}^{j}} \mathbf{F}_{OBm}^{i} \;=\; \sum_{IP=1}^{n_{IP}} \left[\mathbf{R} \cdot \begin{bmatrix} 1 & 0 & 0 \end{bmatrix}^T \, \phi^i \, \phi^j \, \|\mathbf{J}\| \, \mathrm{W}\right]_{IP} \tag{C.7}$$

since

$$\mathbf{t}^T = \begin{bmatrix} -\left(\mathrm{p}'_N + \mathrm{p}_{w3}\right) & \tau_1 & \tau_2 \end{bmatrix}. \tag{C.8}$$

Fluid component

$$\frac{\partial}{\partial \mathrm{p}_{w3}^{j}} \mathrm{F}_{OBf}^{j} \;=\; -\sum_{IP=1}^{n_{IP}} \left[\rho_w \, \mathrm{T}_{w1} \, \phi^i \, \phi^j \, \|\mathbf{J}\| \, \mathrm{W}\right]_{IP}. \tag{C.9}$$

Appendix C.4. Component $[\mathbf{K}]_{16\times 16}^{\Gamma_{\tilde{q}}^{1}\Gamma_{\tilde{q}}^{2}}$ *,* $i = 1, 4$*,* $j = 9, 12$

Mechanical component

$$\frac{\partial}{\partial \mathbf{x}^{j}} \mathbf{F}_{OBm}^{i} \;=\; -\sum_{IP=1}^{n_{IP}} \left[\mathbf{R} \cdot \frac{\partial \mathbf{t}}{\partial \mathbf{x}^{j}} \, \|\mathbf{J}\| \, \phi^i \, \mathrm{W}\right]_{IP} \tag{C.10}$$

and

$$\frac{\partial \mathbf{t}}{\partial \mathbf{x}^{j}} \;=\; \mathbf{D} \cdot [\mathbf{R}]^T \cdot \boldsymbol{\delta} \, \phi^j. \tag{C.11}$$

Appendix C.5. Component $[\mathbf{K}]^{\Omega^3\Gamma^1_{\tilde{q}}}_{4\times 4}$ *,* i*=* $5,8$*,* j*=* $1,4$

Mechanical component

$$\begin{aligned}\frac{\partial}{\partial \mathbf{x}^j}\mathrm{F}^i_{OBf} &= \sum_{IP=1}^{n_{IP}}\left[\left(\frac{\partial}{\partial \mathbf{x}^j}\dot{\mathrm{S}}\,\phi^i - \frac{\partial \mathrm{f}_{wl1}}{\partial \mathbf{x}^j}\nabla_{\mathbf{e}^1_2}\left(\phi^i\right) - \frac{\partial \mathrm{f}_{wl2}}{\partial \mathbf{x}^j}\nabla_{\mathbf{e}^1_3}\left(\phi^i\right)\right)\,\|\mathbf{J}\|\,\mathrm{g}_N\,\mathrm{W}\right]_{IP}\\ &+\sum_{IP=1}^{n_{IP}}\left[\left(\dot{\mathrm{S}}\,\phi^i - \mathrm{f}_{wl1}\nabla_{\mathbf{e}^1_2}\left(\phi^i\right) - \mathrm{f}_{wl2}\nabla_{\mathbf{e}^1_3}\left(\phi^i\right)\right)\,\frac{\partial\|\mathbf{J}\|}{\partial \mathbf{x}^j}\,\mathrm{g}_N\,\mathrm{W}\right]_{IP}\\ &+\sum_{IP=1}^{n_{IP}}\left[\left(\dot{\mathrm{S}}\,\phi^i - \mathrm{f}_{wl1}\nabla_{\mathbf{e}^1_2}\left(\phi^i\right) - \mathrm{f}_{wl2}\nabla_{\mathbf{e}^1_3}\left(\phi^i\right)\right)\,\|\mathbf{J}\|\,\frac{\partial \mathrm{g}_N}{\partial \mathbf{x}^j}\,\mathrm{W}\right]_{IP}\\ &-\sum_{IP=1}^{n_{IP}}\left[\left(\rho_w\,\mathrm{T}_{w1}\,\left(\mathrm{p}_{w1}-\mathrm{p}_{w3}\right)\,\phi^i - \rho_w\,\mathrm{T}_{w2}\,\left(\mathrm{p}_{w3}-\mathrm{p}_{w2}\right)\,\phi^i\right)\,\frac{\partial\|\mathbf{J}\|}{\partial \mathbf{x}^j}\,\mathrm{W}\right]_{IP}\end{aligned} \tag{C.12}$$

where

$$\frac{\partial \mathrm{g}_N}{\partial \mathbf{x}^j} = \begin{bmatrix}1 & 0 & 0\end{bmatrix}\cdot\left(\frac{\partial \mathbf{R}}{\partial \mathbf{x}^j}\cdot\Delta\mathbf{x} + \mathbf{R}\cdot\boldsymbol{\delta}\,\phi^j\right). \tag{C.13}$$

Fluid component

$$\frac{\partial}{\partial \mathrm{p}^j_{w1}}\mathrm{F}^i_{OBf} = -\sum_{IP=1}^{n_{IP}}\left[\rho_w \mathrm{T}_{w1}\,\phi^j\,\phi^i\,\|\mathbf{J}\|\,\mathrm{W}\right]_{IP}. \tag{C.14}$$

Appendix C.6. Component $[\mathbf{K}]^{\Omega^3\Omega^3}_{4\times 4}$ *,* i*=* $5,8$*,* j*=* $5,8$

$$\begin{aligned}\frac{\partial}{\partial \mathrm{p}^j_{w3}}\mathrm{F}^i_{OBf} &= \sum_{IP=1}^{n_{IP}}\left[\frac{\mathrm{k}^l}{\mu_w}\,\left(\nabla_{\mathbf{e}^1_2}\left(\phi^j\right)\,\nabla_{\mathbf{e}^1_2}\left(\phi^i\right) + \nabla_{\mathbf{e}^1_3}\left(\phi^j\right)\,\nabla_{\mathbf{e}^1_3}\left(\phi^i\right)\right)\,\|\mathbf{J}\|\,\mathrm{g}_N\,\mathrm{W}\right]_{IP}\\ &+\sum_{IP=1}^{n_{IP}}\left[\rho_w\,\left(\mathrm{T}_{w1}\,\phi^j + \mathrm{T}_{w2}\,\phi^j\right)\,\phi^i\,\|\mathbf{J}\|\,\mathrm{W}\right]_{IP}.\end{aligned} \tag{C.15}$$

Appendix C.7. Component $[\mathbf{K}]^{\Omega^3\Gamma^2_{\tilde{q}}}_{4\times4}$ *,* i*=* $5,8$*,* j*=* $9,12$

Mechanical component

$$\begin{aligned}\frac{\partial}{\partial \mathbf{x}^j}\mathrm{F}^i_{OBf} &= \sum_{IP=1}^{n_{IP}}\left[\left(\frac{\partial}{\partial \mathbf{x}^j}\dot{\mathrm{S}}\,\phi^i - \frac{\partial \mathrm{f}_{wl1}}{\partial \mathbf{x}^j}\nabla_{\mathbf{e}^1_2}\left(\phi^i\right) - \frac{\partial \mathrm{f}_{wl2}}{\partial \mathbf{x}^j}\nabla_{\mathbf{e}^1_3}\left(\phi^i\right)\right)\|\mathbf{J}\|\,\mathrm{g}_N\,\mathrm{W}\right]_{IP}\\ &+\sum_{IP=1}^{n_{IP}}\left[\left(\dot{\mathrm{S}}\,\phi^i - \mathrm{f}_{wl1}\nabla_{\mathbf{e}^1_1}\left(\phi^i\right) - \mathrm{f}_{wl2}\nabla_{\mathbf{e}^1_2}\left(\phi^i\right)\right)\frac{\partial\|\mathbf{J}\|}{\partial \mathbf{x}^j}\,\mathrm{g}_N\,\mathrm{W}\right]_{IP}\\ &+\sum_{IP=1}^{n_{IP}}\left[\left(\dot{\mathrm{S}}\,\phi^i - \mathrm{f}_{wl1}\nabla_{\mathbf{e}^1_2}\left(\phi^i\right) - \mathrm{f}_{wl2}\nabla_{\mathbf{e}^1_3}\left(\phi^i\right)\right)\|\mathbf{J}\|\frac{\partial \mathrm{g}_N}{\partial \mathbf{x}^j}\,\mathrm{W}\right]_{IP}\\ &-\sum_{IP=1}^{n_{IP}}\left[\left(\rho_w\,\mathrm{T}_{w1}\,(\mathrm{p}_{w1}-\mathrm{p}_{w3})\,\phi^i - \rho_w\,\mathrm{T}_{w2}\,(\mathrm{p}_{w3}-\mathrm{p}_{w2})\,\phi^i\right)\frac{\partial\|\mathbf{J}\|}{\partial \mathbf{x}^j}\,\mathrm{W}\right]_{IP}.\end{aligned} \tag{C.16}$$

Fluid component

$$\frac{\partial}{\partial \mathrm{p}^j_{w2}}\mathrm{F}^i_{OBf} = \sum_{IP=1}^{n_{IP}}\left[\rho_w\,\mathrm{T}_{w2}\,\phi^j\,\phi^i\,\|\mathbf{J}\|\,\mathrm{W}\right]_{IP}. \tag{C.17}$$

Appendix C.8. Component $[\mathbf{K}]^{\Gamma^2_{\tilde{q}}\Gamma^1_{\tilde{q}}}_{16\times16}$ *,* i*=* $9,12$*,* j*=* $1,4$

Mechanical component

$$\frac{\partial}{\partial \mathbf{x}^j}\mathbf{F}^i_{OBm} = \sum_{IP=1}^{n_{IP}}\left[\frac{\partial}{\partial \mathbf{x}^j}\left(\|\mathbf{J}\|\,\mathbf{R}\right)\cdot\mathbf{t}\,\phi^i\,\mathrm{W} + \mathbf{R}\cdot\frac{\partial\,\mathbf{t}}{\partial \mathbf{x}^j}\,\|\mathbf{J}\|\,\phi^i\,\mathrm{W}\right]_{IP} \tag{C.18}$$

and

$$\frac{\partial \mathbf{t}}{\partial \mathbf{x}^j} = \mathbf{D}\cdot\left(\mathbf{S}^T\cdot\Delta\dot{\mathbf{x}} - [\mathbf{R}]^T\cdot\boldsymbol{\delta}\,\phi^j\right). \tag{C.19}$$

Appendix C.9. Component $[\mathbf{K}]^{\Gamma^2_{\tilde{q}}\Omega^3}_{16\times4}$ *,* i*=* $9,12$*,* j*=* $5,8$

Coupling component

$$\frac{\partial}{\partial \mathrm{p}^j_{w3}}\mathbf{F}^i_{OBm} = -\sum_{IP=1}^{n_{IP}}\left[\mathbf{R}\cdot\begin{bmatrix}1 & 0 & 0\end{bmatrix}^T\phi^i\,\phi^j\,\|\mathbf{J}\|\,\mathrm{W}\right]_{IP}. \tag{C.20}$$

Fluid component

$$\frac{\partial}{\partial \mathrm{p}^j_{w3}}\mathrm{F}^j_{OBf} = -\sum_{IP=1}^{n_{IP}}\left[\rho_w\,\mathrm{T}_{w2}\,\phi^i\,\phi^j\,\|\mathbf{J}\|\,\mathrm{W}\right]_{IP}. \tag{C.21}$$

Appendix C.10. Component $[\mathbf{K}]^{\Gamma_q^2 \Gamma_q^2}_{16\times 16}$ *,* i= 9, 12, j= 9, 12

Mechanical component

$$\frac{\partial}{\partial \mathbf{x}^j}\,\mathbf{F}^i_{OBm} \;=\; \sum_{IP=1}^{n_{IP}} \left[\mathbf{R}\cdot\frac{\partial\,\mathbf{t}}{\partial \mathbf{x}^j}\,\|\mathbf{J}\|\,\phi^i\,\mathrm{W}\right]_{IP} \tag{C.22}$$

and

$$\frac{\partial \mathbf{t}}{\partial \mathbf{x}^j} \;=\; \mathbf{D}^{ep}\cdot[\mathbf{R}]^T\cdot\boldsymbol{\delta}\,\phi^j. \tag{C.23}$$

Fluid component

$$\frac{\partial}{\partial \mathrm{p}^j_{w2}}\,\mathbf{F}^i_{OBf} \;=\; \sum_{IP=1}^{n_{IP}} \left[\rho_w\,\mathrm{T}_{w2}\,\phi^j\,\phi^i\,\|\mathbf{J}\|\,\mathrm{W}\right]_{IP}. \tag{C.24}$$